

博士論文（要約）

Three-dimensional numerical optimization of solid
oxide fuel cell cathode microstructure
(固体酸化物形燃料電池空気極微細構造の
三次元数値最適化)

何 岸

Contents

Abstract	iii
Nomenclature	v
Chapter 1 Introduction	1
1.1 Background	2
1.2 Fuel cells	5
1.3 Solid oxide fuel cells	7
1.4 Materials of the solid oxide fuel cell	8
1.4.1 Electrolyte material	8
1.4.2 Anode material	9
1.4.3 Cathode material	10
1.5 Microstructures of the solid oxide fuel cell electrode	13
1.6 Numerical simulations	17
1.6.1 Electrochemical simulations	17
1.6.2 Optimization methods	19
1.7 Objectives of the present study	21
Chapter 2 Numerical Optimization of Porous LSCF Microstructure	1
2.1 Computational domain for optimization model	2
2.2 Governing equations	3
2.2.1 Ionic conductivities	4
2.2.2 Electrochemical reactions	5
2.2.3 Validation	7
2.3 Optimization	8
2.3.1 Objective function and Lagrangian function	8
2.3.2 Optimization procedures	9
2.4 Computational results	17
2.4.1 Optimization from FIB-SEM microstructure	17
2.4.2 Optimization results with different initial microstructures	27
2.4.3 Influence of $i_{0,DPB}$ on optimization results	37
Chapter 3 Effects of Micro GDC pillars in pure LSCF and LSCF-GDC Cathodes	44
3.1 Experiment	45
3.1.1 Fabrication of samples	45
3.1.2 Observation with FIB-SEM	45
3.1.3 Shrinking the particle sizes	45
3.1.4 Reconstruction of the microstructures with GDC pillars	49
3.2 Numerical simulation	51
3.2.1 Electron and ion transport equations	51
3.2.2 Gas transport equation	52
3.2.3 Electrochemical reactions	53
3.2.4 LBM model	54
3.2.5 Validation	55

3.3 Computational results	58
3.3.1 Effects of cathode composition and particle size	58
3.3.2 Effects of GDC pillars on electrochemical performance.....	63
Chapter 4 Numerical Optimization of Electrode-electrolyte Interface Structure.....	71
4.1 Computational domain for optimization model	72
4.2 Governing equations	73
4.2.1 Ionic conductivities	74
4.2.2 Electrochemical reactions	75
4.2.3 Validation	79
4.3 Optimization.....	83
4.3.1 Objective function and Lagrangian function.....	83
4.3.2 Optimization procedures	84
4.4 Optimization of electrode-electrolyte interface shape for pure LSCF cathode	92
4.4.1 Computational parameters	92
4.4.2 Optimization results with different computational domains and with different initial structures.	94
4.5 Optimizations with different electrochemical parameters.....	109
4.5.1 Dimensionless parameters.....	109
4.5.2 Influence of electrolyte conductivity.....	114
4.5.3 Influence of electrode region reaction	118
4.5.4 Influence of interface reaction.....	126
Chapter 5 Conclusions	131
References.....	134
Acknowledgements.....	143

Abstract

In the present study, the optimal structure of $\text{La}_{0.6}\text{Sr}_{0.4}\text{Co}_{0.2}\text{Fe}_{0.8}\text{O}_3$ (LSCF) phase inside the pure LSCF cathode is obtained using an adjoint method. Then, the electrochemical effects of $\text{Gd}_{0.1}\text{Ce}_{0.9}\text{O}_{2-\delta}$ (GDC) pillars inside the LSCF cathode is numerically investigated. Finally, the numerical optimization of the electrode-electrolyte interface shape is conducted.

Adjoint method is applied to optimize the structure of LSCF phase inside the pure LSCF cathode. The optimization is conducted until the total amount of reaction current density in the whole computational domain is maximized. During optimization, the FIB-SEM microstructure is optimized into the microstructure composed of LSCF particles with smaller particle sizes. The volume fraction of LSCF phase inside the optimized structure reduces along the thickness direction, and this gradient becomes larger for larger DPB reaction exchange current density ($i_{0,\text{DPB}}$). The LSCF is optimized into the microstructure composed of LSCF nano-particles even starting from dense LSCF pillars which is completely different from porous LSCF microstructures. The structure transformation of LSCF-pore interface mainly takes place at the electrolyte side. This is because the gradient of ionic potential is concentrated at the electrolyte side, and the regions near the electrolyte side is more important for the electrochemical performance than the region near the current collector side. This indicates that the porous LSCF microstructures are the best microstructure which can maximize the cell performance. What is more, the size of LSCF particles is the same even for different initial structures, which also implies that the particle size is crucial to enhance the cell performance.

In order to investigate the electrochemical effects of GDC pillars inside the LSCF cathode, three-dimensional pure LSCF and LSCF-GDC composite cathode microstructures with different particle sizes are reconstructed by focused ion beam scanning electron microscopy (FIB-SEM), and the GDC pillars with different pillar lengths are inserted into these microstructures. According to the numerical simulation, it is shown that the GDC pillars can improve the cell performance by expanding the reactive thickness and by improving the ionic conductivities. The performance improvement is more pronounced for smaller particles, because the GDC pillars can expand the reactive regions more effectively for the microstructure with small particle size. In addition, the performance improvement is more pronounced for pure

the LSCF cathode than the LSCF-GDC composite, because the GDC pillars more efficiently improve the effective conductivity for pure LSCF cathodes. In addition, if the GDC pillar is too long, the pillars replace the electrode region which is originally conductive, and the performance improvement effect is suppressed.

In order to optimize the shape of the interface between cathode and electrolyte, the computational domain is divided into the electrolyte region and electrode region. In the electrode region, electrode phase and pore phases are assumed to be homogeneously distributed. The electrolyte region is composed of electrolyte materials with high ionic conductivity. Electrochemical reactions are assumed to take place at both electrode region and electrode-electrolyte interface. The interface shape between the pure LSCF cathode and GDC electrolyte is first optimized. It is found that the cathode with optimized interface structure has better electrochemical performance than the microstructure with flat interface. In addition, the volume of optimized electrolyte region structure is independent from the computational domain and the initial microstructure shapes.

In order to give guidance to the microstructure design with various electrolyte materials and with various electrode microstructures, the influence of dimensionless numbers on the optimized microstructure is investigated. It is analyzed that the distribution of ionic electrochemical potential is controlled by three dimensionless numbers, k , $\Gamma_{\text{electrode}}$, and $\Gamma_{\text{interface}}$. The change in the dimensionless number k is realized by changing electrolyte ionic conductivity ($\sigma_{\text{O}^{2-}, \text{electrolyte}}$). The optimized electrolyte region size becomes smaller with larger $\sigma_{\text{O}^{2-}, \text{electrolyte}}$. The change in the dimensionless number $\Gamma_{\text{electrode}}$ is realized by changing the electrode region reaction coefficient ($\beta_{\text{electrode}}$). The optimized electrolyte region size becomes larger with larger $\beta_{\text{electrode}}$. This is because the reactive thickness of the microstructure becomes thinner with larger $\beta_{\text{electrode}}$. The change in the dimensionless number $\Gamma_{\text{interface}}$ is realized by changing the interface reaction coefficient ($\beta_{\text{interface}}$). The optimized electrode-electrolyte interface area becomes larger with larger $\beta_{\text{interface}}$.

Nomenclature

Roman symbols

i_{reac}	Reaction current (A/m ³)
F	Faraday constant (C/mol)
f_i	Velocity distribution function
i	Current density (A/m ²)
T	Temperature (°C)
D_v	Vacancy diffusion coefficient
D	Diffusion coefficient (m ² /s)
C_{O_2}	Oxygen concentration (mol/m ³)
$i_{0,\text{TPB}}$	TPB reaction exchange current density (A/m)
$i_{0,\text{DPB}}$	DPB reaction exchange current density (A/m ²)
L_{TPB}	TPB length density (m/m ³)
A_{DPB}	DPB area density (m ² /m ³)
p_{O_2}	Oxygen partial pressure (Pa)
w	Source term
R	Gas constant (J/K·mol)

Greek symbols

σ	Conductivity (S/m)
Ω_D	Collision integral
ζ	Intermolecular force constant (Å)
η	Overpotential (V)
ϕ	Level set function
ψ	Heaviside function based on level-set function.
δ	Dirac delta function based on level-set function.
ξ	Coefficient in Heaviside function or Dirac delta function.
ρ_{DPB}	DPB area density during optimization (m ² /m ³)
ρ_{TPB}	TPB length density during optimization (m/m ²)
J_c	Objective function to be maximized during simulation.
β	Coefficient for linearized Butler-Volmer equation.
\mathcal{L}	Lagrangian cost function
$\tilde{\mu}$	Electrochemical potential (J/mol)
$\tilde{\mu}_{\text{O}^{2-}}^*$	Adjoint variable of electrochemical potential
τ_l	Discrete fictitious time increment for updating the level-set function.

Chapter 1

Introduction

1.1 Background

People consume energy in various aspects of human activities, from daily life to products manufacturing [1-3]. As estimated by the world bank that in 2015, 80.04 % of world energy consumption comes from the fossil fuels[4], and 65% of the world's electrical energy used today is generated by steam turbine generators burning fossil fuels as their source of energy[5]. However, increasing consumption of the fossil fuels causes social problems of energy shortage and environment issues.

Fossil fuel consumption leads to the problem of energy shortage. As the form of nonrenewable energy resources, the fossil fuels existing on earth are not infinite. As shown in Fig. 1-1, with the assumption that the world energy consumption rate is maintained in the following decades, the estimated remaining years of extraction will be 114 years for coal, 52.8 years for natural gas, and 50.7 years for crude oil [6].

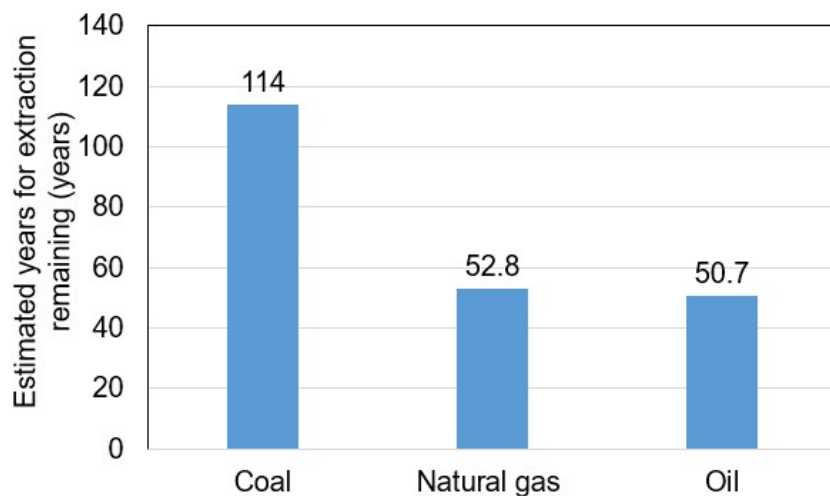


Fig. 1-1 Remaining years of extraction of multiple types of fuel [6].

Energy consumption also leads to environmental issues. Before industrial revolution, atmosphere carbon dioxide concentrations increased in a rather steady rate [7], human activities exerted little influences on the natural environment. With industrialization, the carbon dioxide concentration in the atmosphere has been increased drastically. It is estimated that in 2013, the world average concentration of

carbon dioxide has increased about 40% since the pre-industrialized era; methane and nitrous oxides levels have also increased significantly during last century [7]. It is reported that more than 60% of greenhouse gas emissions are from fuel combustion[7], and today's situation is so serious that even if the carbon dioxide concentration kept constant, global warming and sea level rise would still continue because of climate feedbacks [8]. In order to relieve the environmental burden of nature, Japanese government decided to cut its greenhouse gas emissions by 26 percent by 2030 [9].

Nowadays, common practices to solve the problems caused by fossil fuel consumption involve: 1 using sustainable energy systems, and 2 application of high efficiency energy generation systems.

For the sustainable energy, the nuclear power station, the wind energy system, and the solar energy system are commonly used. Nuclear power sources attract attention because of its large amount of reservation. It is estimated that, under current world consumption rate, remaining uranium reservation can supply for more than 200 years [10]. However, nuclear power systems are always questioned for its safety issue. As shown in Fig. 1-2, the Japanese nuclear power generation decreases dramatically because of the accident in Fukushima in 2011 [11]. The wind energy is known for its infinite amount but unsteady characteristics. Although people are trying to harness the wind energy before the industrial revolution, until today, the wind energy system still cannot fully overcome the unsteadiness of the wind, and the facilities for wind power stations remain expensive [12]. Besides, the wind energy is highly geo-selective, which indicates that different domains and different climates have completely different abilities to generate wind power. Moreover, the wind power stations will cause huge damage to wildlife and habitat [13]. The solar energy is one of the most sustainable and cleanest types of energy. Now engineers have already harnessed the solar energy to heat water, run calculators, and even fly airplanes. However, there are also criticisms about solar systems; (1) solar panel manufacture will cause contamination to the environment, (2) solar power is highly dependent on local climate, and the generation of power is not steady enough [14].

Considering today's social and technical improvements, mid-term and most

promising solution for energy shortage and environmental issue is to improve the power efficiency and make the power systems environmental-friendly. The fuel cell is one of the popular choice of these novel power systems [15,16].

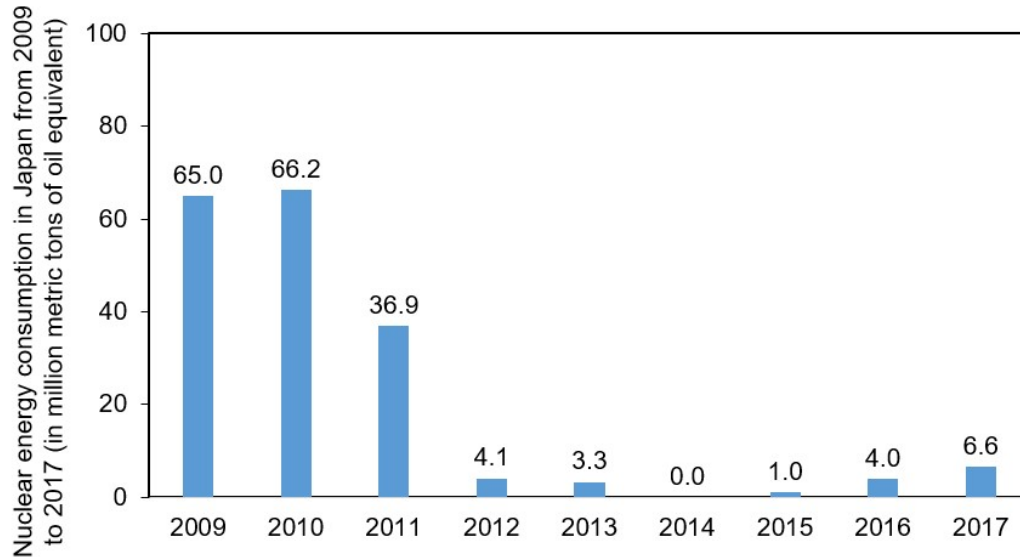


Fig. 1-2 Nuclear energy consumption in Japan from 2009 to 2017 (in million metric tons of oil equivalent) [11].

1.2 Fuel cells

Traditionally, in order to obtain electric energy, multiple steps of energy conversion processes are required inside the fossil-fuel power station. Chemical energy of natural gas, oil and coal is firstly converted into thermal energy through combustion; then thermal energy is transferred to the internal energy of the steam; and steam energy is converted into mechanical energy by forcing the gas turbine; finally, the mechanical energy is transformed into the electrical energy. Among them, conversion of chemical energy into thermal energy by combustion causes huge exergy loss and sacrifices the energy converting efficiency, the energy efficiency for the traditional fossil fuel power station remains low[17].

As for the fuel cell system, the chemical energy of the fuels is directly converted into the electric energy, and total efficiency of the power plant is largely enhanced compared with the traditional fossil fuel power station. Moreover, during the fuel cell operation, there is no emission of the nitrogen oxides, which indicates that the by-products are eco-friendly. There are four main types of fuel cells, i.e. the proton exchange membrane fuel cell (PEMFC), the molten carbonate fuel cell (MCFC), the phosphoric acid fuel cell (PAFC), and the solid oxide fuel cell (SOFC).

The PEMFC is composed of an aqueous acidic polymer membrane and platinum-based electrodes. It is prospective in vehicles and light duty power station because of its low operation temperature and high energy efficiency. However, the PEMFC is criticized for its high catalyst expenses and the fuel inflexibility [17].

The molten carbonate fuel cell (MCFC) is composed of the electrodes that use non-noble metal as the catalyst and the electrolyte which is a molten carbonate salt suspended in a porous ceramic matrix. In order to maintain reaction kinetics and reduce poisoning, the MCFC operates at high temperature (about 650°C). The disadvantage of the MCFC is the corrosion because of the high temperature molten salt [18].

The phosphoric acid fuel cell (PAFC) is composed of the electrodes made of platinum catalyst and the electrolyte made of phosphoric acid. The PAFC has a long operation time because of its resistance against poisoning by carbon monoxide, and

therefore, the PAFC is widely used in stationary power stations. However, the disadvantage of the PAFC is that the PAFC possesses relatively low efficiency. [19]

The solid oxide fuel cell (SOFC) is usually composed of ceramics electrolyte, metal oxide based electrodes. The solid oxide fuel cell is characterized by high operation temperature (600°C-1000°C) and high energy efficiency. Additionally, the SOFC is flexible with hydrocarbon fuels because oxide ion transfers through the electrolyte [16, 20].

Table 1-1 lists the main characteristics of the four main types of fuel cells.

Table 1-1 Characteristics of four main types of fuel cells.

	PEMFC	MCFC	PAFC	SOFC
Electrolyte material	Proton exchange membrane	Molten carbonate salt	Phosphoric acid	Ceramics
Catalyst	Platinum	No noble metal catalyst	Platinum	No noble metal catalyst
Fuel	Hydrogen	Coal gas, natural gas	Natural gas	hydrocarbon gas, hydrogen
Operation temperature	100°C	600-700°C	170-200°C	600-1000°C
Transferring ion	H ⁺	CO ₃ ²⁻	H ⁺	O ²⁻

1.3 Solid oxide fuel cells

The SOFC is usually composed of highly ionic conductive electrolyte, and porous ceramics electrodes which are both ionic and electronic conductive [21].

Since the solid oxide fuel cell is composed of solid phase material, it can be constructed by multiple structures, such as planer and tubular. The basic structure for the SOFC is that a solid ceramic electrolyte is set in between an anode and a cathode.

As shown in Fig. 1-3, the fuel and the air are flowing into the porous anode and cathode of the SOFC, respectively. Under high operation temperature, the electrochemical reactions take place in the reactive regions in the electrodes. In the anode side, the fuel and the oxide ions are consumed, while water and electrons are produced. In the cathode side, the oxygen and the electrons are consumed while the oxide ions are generated.

Anode reaction: $\text{H}_2 + \text{O}^{2-} \rightarrow \text{H}_2\text{O} + 2\text{e}^-$, $\text{CO} + \text{O}^{2-} \rightarrow \text{CO}_2 + 2\text{e}^-$;

Cathode reaction: $\text{O}_2 + 4\text{e}^- \rightarrow 2\text{O}^{2-}$

It should be noted that the electrochemical reactions of the electrodes take place at the regions where the gas phase, the electron phase, and the oxide ion phase all exist.

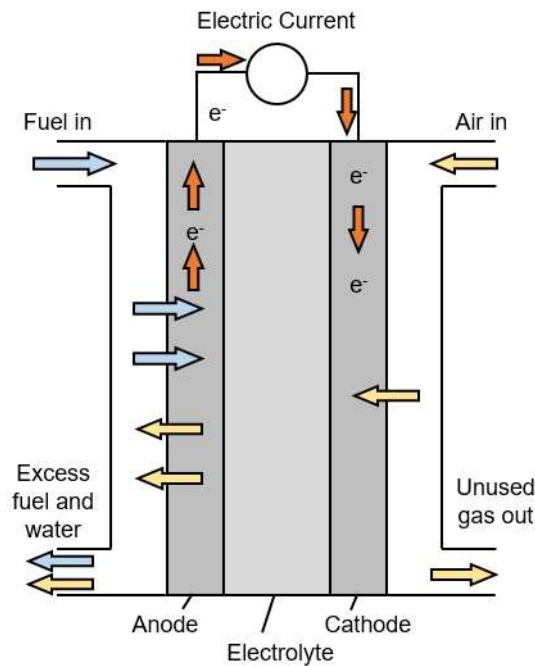


Fig. 1-3 Schematic of SOFC.

1.4 Materials of the solid oxide fuel cell

1.4.1 Electrolyte material

The electrolyte is sandwiched by the two electrodes [21], which transfers oxide ion from the cathode to the anode in order to maintain overall electrical charge balance. Accordingly, the electrolyte material should be highly ionic conductive at the SOFC operation conditions.

Yttria-stabilized zirconia (YSZ) is the most commonly used electrolyte material for its high ionic conductivity at high operation temperature (over 800 °C) [22- 25]. The YSZ is fabricated by adding yttrium into zirconia. The crystalline microstructure of ZrO_2 has two oxide ions to one metal ion, while in Y_2O_3 , there are only 1.5 oxide ions to the metal ion [21]. In the microstructure of the YSZ, the Y_2O_3 is distributed inside the microstructure of ZrO_2 , so there remain plenty of structural vacancies where oxide ions are missing. During conduction, oxide ions can move through the vacancies inside the crystal structure.

However, high operation temperature (over 800 °C) significantly limits the choice of the component materials [26-30]. Reduction of the SOFC operation temperature is attractive for its ability to reduce the system cost and to enhance the cell durability [26]. Thus, developing of the SOFC which is able to operate under intermediate temperature (500-800 °C) is attractive. At intermediate operation temperature of the SOFC (600-800°C), the ionic conductivities of the YSZ material dramatically decreases, which makes it an unideal choice for the electrolyte material at the intermediate operation temperatures. Gadolinium doped ceria (GDC) [26] is one of the choices because of its high ionic conductivity and good electrochemical reaction properties even at intermediate operation temperature conditions.

1.4.2 Anode material

Inside the anode, hydrogen gas is diffused inside the porous microstructure. Through the electrochemical reaction, oxide ion reacts with hydrogen and release electron, and the electrons are transported to the current collector. With the existence of electromotive force, electric power can be utilized in the external circuit. Because of the electrochemical effects of the anode electrode, the material characterized with high ionic conductivity and good electrochemical reaction properties is desirable.

Ni-YSZ is the most commonly used anode material in the SOFC because of its high conduction properties and good reactive properties at high operation temperature [23,31]. The electron conducts in the Ni phase, the oxide ion conducts in the YSZ phase,

while the gas is transported in the pore phase. The electrochemical reaction takes place with the existence of the electron, oxide ion, and gases. Therefore, the reaction takes place in the triple phase boundary (TPB) as shown in Fig. 1-4. Typically, a Ni volume fraction of 30% is required to achieve a good anode electronic conductivity. However, the Ni-YSZ anode is criticized for its poor redox stability, low Sulphur tolerance, and tendency of nickel agglomeration after long-time operation [32].

Tao and Irvine [32] introduced $\text{La}_{0.75}\text{Sr}_{0.25}\text{Cr}_{0.5}\text{Mn}_{0.5}\text{O}_3$ (LSCM) anode and demonstrated that LSCM cathode has redox stable characteristics and good electrochemical properties in low steam hydrocarbons. However, LSCM has a low electronic conductivity in the reducing atmosphere and is not stable to sulfur impurities in the fuel. Other types of nickel-free anodes have been developed, such as $\text{La}_{0.3}\text{Sr}_{0.7}\text{Fe}_{0.7}\text{Cr}_{0.3}\text{O}_3$ (LSFCr) [33,34], $\text{YSZ-Sr}_{0.88}\text{Y}_{0.08}\text{TiO}_3$ (YST) [35], and $\text{Sr}_2\text{MgMoO}_6$ (SMM) [36]. What is more, it is reported that the addition of GDC particles into the LSCM anode largely improves the anode performance by enhancing the electrochemical reaction properties [37].

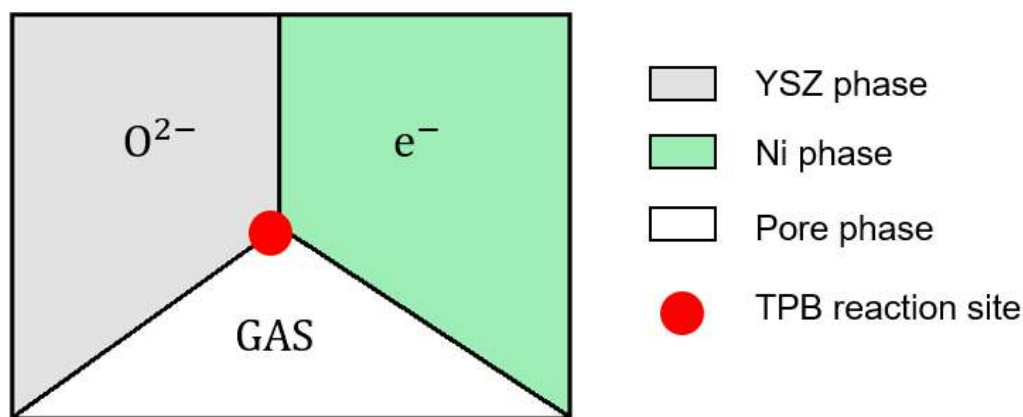


Fig. 1-4 Triple phase boundary reaction scheme for Ni-YSZ anode.

1.4.3 Cathode material

Inside the cathode, oxygen gas is diffused inside the micro pores. The electrons from the external circuit react with oxygen gas, and oxide ions are incorporated into the cathode material.

The common cathode materials are the perovskite-type lanthanum strontium manganite, LaSrMnO_3 (LSM) [38] and the lanthanum calcium manganite, LaCaMnO_3 (LCM) [43]. These materials are able to provide good thermal expansion match with zirconia based electrolyte materials, and possess good electronic conductive property [21].

As for intermediate temperature, oxygen reduction characteristics of LSM and LCM degrade a lot under intermediate temperature range, and therefore, these materials are no longer effective. Thus, at intermediate temperature, materials such as lanthanum strontium cobaltite ferrite (LSCF) [26, 39,40-42] are commonly used in the SOFC cathode electrode because they present fast oxygen reduction kinetics, large ionic and electronic conductivities and good thermal expansion match with GDC. What is more, LSC and LSCF are characterized as mixed ionic and electronic conductors (MIEC). At the LSC/pore and LSCF/pore surface, the chemical reaction is able to take place with the coexistence of oxide ion, electron and gas phases, which largely increases the reactive domain as shown in Fig. 1-5 (b) [27,28,40]. It is also demonstrated that the addition of highly ionic conductive materials, such as GDC particles, in the LSCF or LSC microstructures largely improve the electrochemical performances [27,28,40,43,44]. This is because the LSCF and LSC cathode has relatively low oxide ion conductivities, while the addition of GDC phase enhances the effective ionic conductivity. Kim et al. [40] suggested that the addition of GDC phase introduces the GDC/LSCF/pore triple phase boundary reaction as shown in Fig. 1-5 (c), which improves the reaction properties of the electrode.

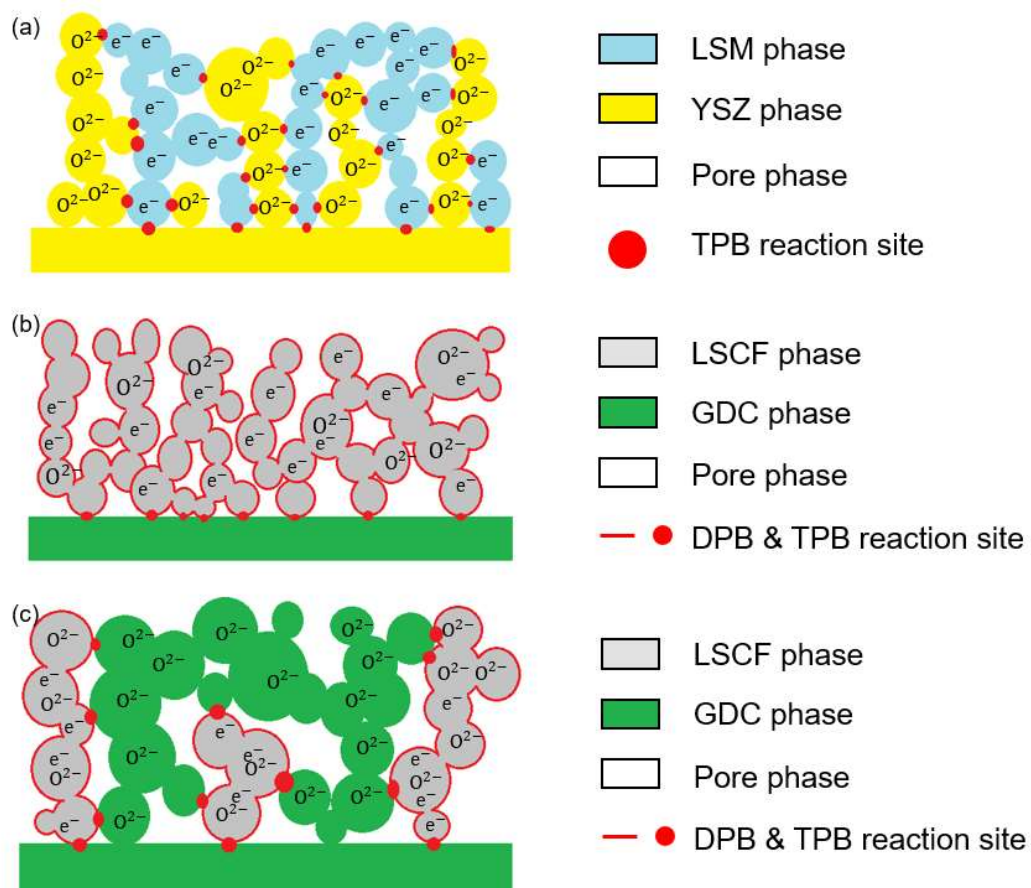


Fig. 1-5 Reaction scheme for (a) LSM-YSZ, (b) pure LSCF, and (c) LSCF-GDC cathode.

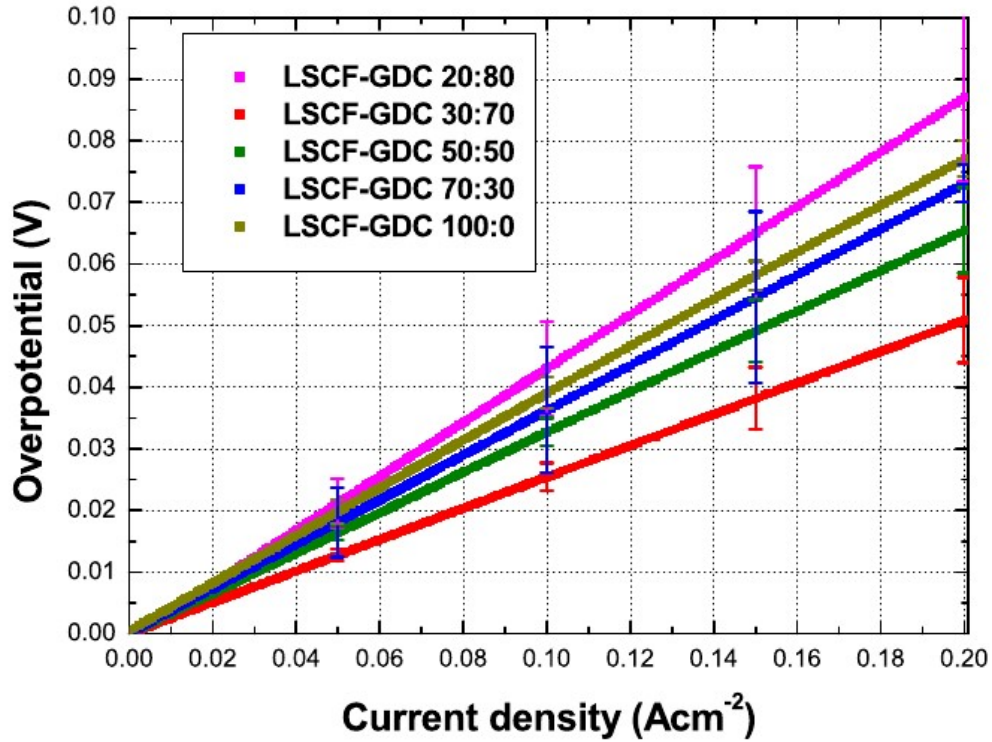


Fig. 1-6 Overpotentials for different LSCF-GDC cathodes by Kim et al. [27].

1.5 Microstructures of the solid oxide fuel cell electrode

The gas, oxide ions, and the electrons transfer [21,26], as well as electrochemical reactions take place in the electrodes of the solid oxide fuel cells. The geometries of the SOFC electrode microstructures are of great importance to the electrochemical performance. Optimization of the microstructure of the SOFC electrode can largely improve the cell performance by affecting the transport and reaction properties.

To maximize the reaction site density, microstructures with small particle sizes are proposed [45]. As shown in Fig. 1-7, the TPB densities are largely improved by reducing the particle size of the Ni-YSZ anode. Figures 1-5 and 1-6 show the SEM images for small particle sized electrode in Ref. [45]. Sato et al. [46] used nano-sized LSCF-GDC composite cathode during operation, and low area specific polarization resistance is obtained for the electrode microstructure with small particle sizes.

Poor conductivities and the improved reaction properties decrease the reactive

thickness of the SOFC electrode, as shown in Fig. 1-9 (a). For conventional electrode microstructures, the reactive regions are concentrated at the vicinity closed to the electrolyte regions. Highly ionic conductive pillar is expected to improve the electrochemical performance. Nagato *et al.* [47] inserted nanopowders of Ni into the YSZ electrolyte substrate with pillars, and it is concluded that YSZ pillars improve the electrochemical performance. Delloro and Viviani [48] numerically verified that the cell performance of the SOFC can be largely improved with the addition of highly ionic conductive pillars.

According to Bertei *et al.* [49], YSZ pillars can effectively enhance the effective ionic conductivity for the Ni-YSZ electrodes. However, the electrode structure applied by Bertei *et al.* was simplified into a 2D structure, and the structural parameters were homogeneously distributed throughout the computational domain, thus the three-dimensional structural details were not fully considered. What is more, only one type of Ni-YSZ anode structure is applied during the investigation of Bertei *et al.* While the electrochemical effect of pillar is to be varied with various of electrode microstructures. Therefore, a full understanding of the pillar effect requires the investigation of different electrode structures.

Okabe *et al.* [50] used UV-nanoimprint lithography to fabricate ceramic electrolyte with micro pillars with diameter as small as 10 μm , which suggests that if the shape of the pillar is fully optimized, the optimized microstructure can be realized with current fabrication techniques.

Not only for highly conductive pillars, many other electrode microstructures have been applied in order to achieve better performance. As shown in Fig. 1-10, LSCF nanofibers microstructures were used as the cathode to provide continuous ionic conduction for the electrode microstructures and to increase the reaction site densities [51]. As shown in Fig. 1-11, maximum power density of 0.99 W cm^{-2} at 600 $^{\circ}\text{C}$ is achieved for the cathode with small LSCF grain size [52]. However, the optimal structure of the electrodes is still unknown, the optimization of the electrode microstructure is expected to give good guidance for the SOFC design.

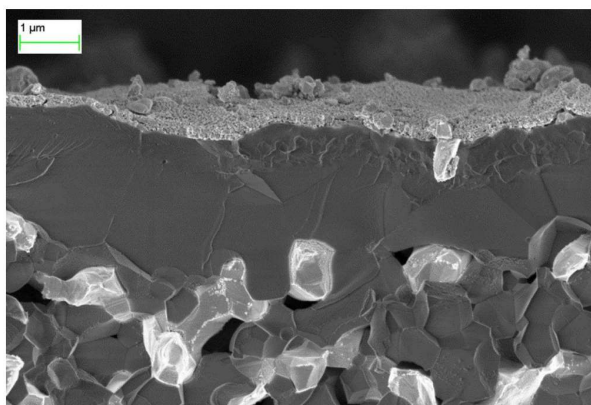


Fig. 1-5 Cross-section of the nano-scaled Ni-YSZ anode [45].

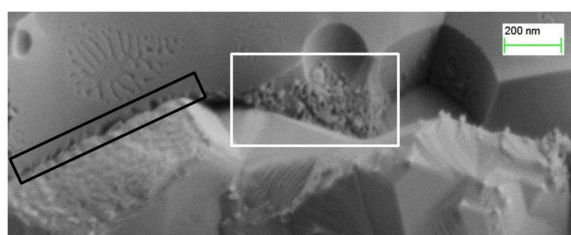


Fig. 1-6 Interface between the electrolyte and the anode. White rectangle is the YSZ mixed with the nickel; black rectangle is the porous nano-scaled layer between the electrolyte and the anode [45].

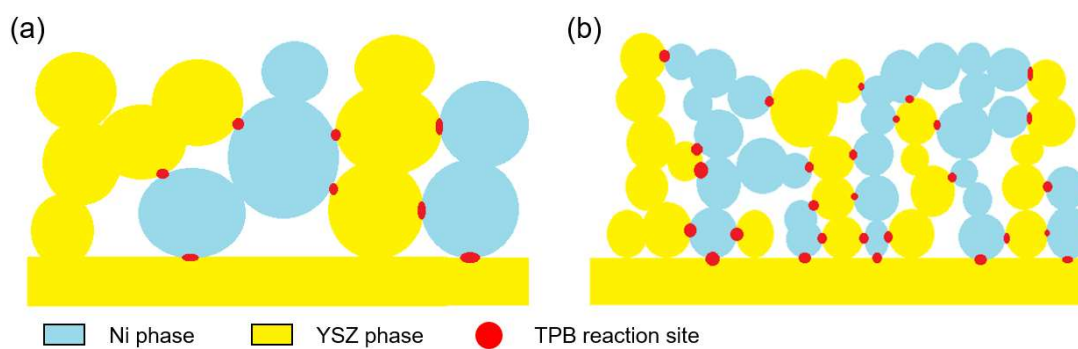


Fig. 1-7 (a) Ni-YSZ anode microstructure with larger particle sizes, and (b) Ni-YSZ anode microstructure with smaller particle size.

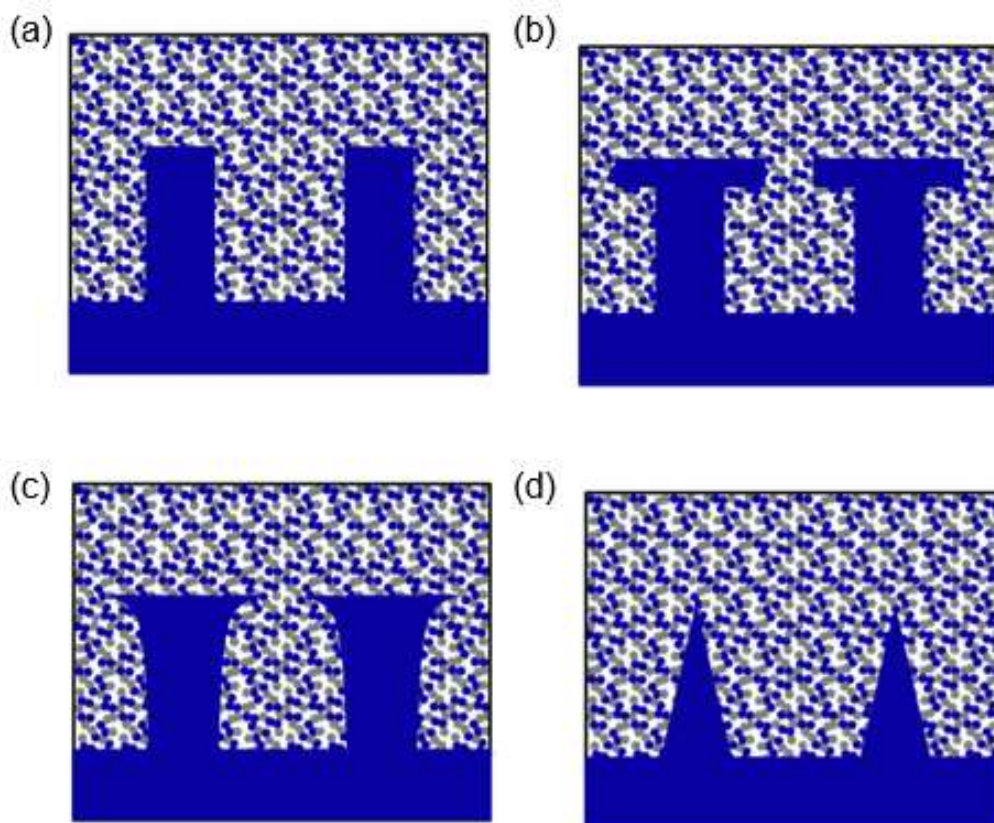


Fig. 1-8 Different pillar shapes applied in Bertei et al.: (a) rectangular pillar, (b) pillar with terrace, (c) rounded terrace, and (d) triangular pillar. [49]

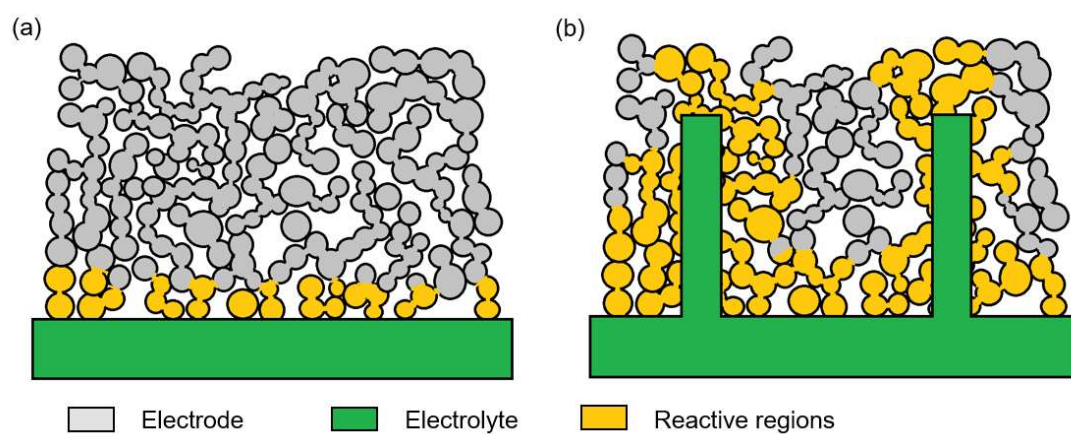


Fig. 1-9 (a) The scheme of reactive regions for the conventional microstructures, and (b) the scheme of the reactive regions for the microstructure with highly ionic conductive pillars. [84]

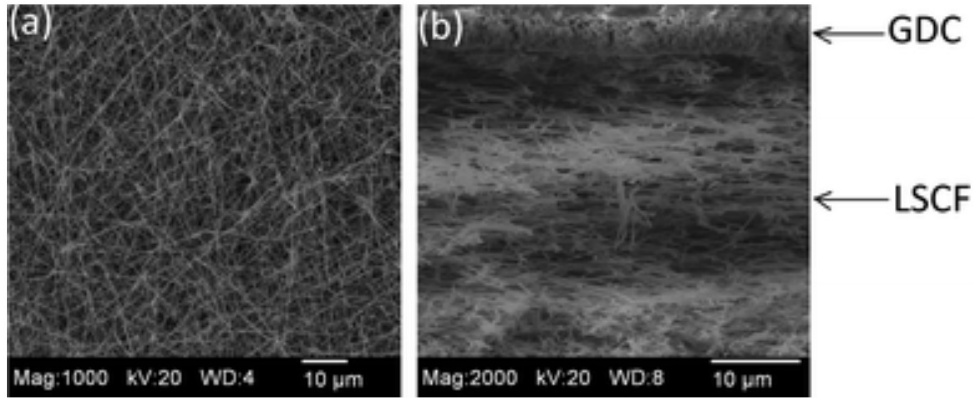


Fig. 1-10 SEM images of the LSCF nano fiber cathode: (a) top view of the cathode, and (b) cross-section of the cathode. [51]

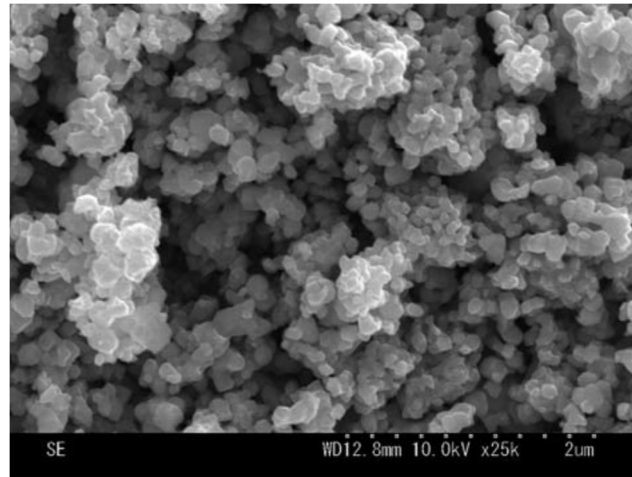


Fig. 1-11 Cross-sectional SEM microstructure of the LSCF cathode [52] .

1.6 Numerical simulations

1.6.1 Electrochemical simulations

Solid oxide fuel cells performances are related with the electrode electrochemical reaction properties and the gaseous, electronic and ionic transport properties. Numerical models are often used to explain the intrinsic mechanism, and to predict the electrochemical system. An accurate and fast prediction will lead to efficient developments of new designs and manufacturing methods in the SOFC field [53,54].

The SOFC simulation is often based on reconstructed microstructures. Traditionally, the SOFC simulation is conducted with two dimensional microstructures based on the images taken by the scanning electron microscopy (SEM) [53]. For example, traditionally, researchers approximated the tortuosity factor of the microstructure from the porosity using Bruggemann's equation [55]. However, as the 3D geometric details are not considered, the computational accuracy is sacrificed. Recently, dual beam focused ion beam-scanning electron microscopy (FIB-SEM) is used to obtain the three-dimensional microstructures of the SOFC electrodes [56]. Using three-dimensional microstructures, the numerical simulations can provide more informative results.

Gostovic *et al.* [57] investigated the cathode surface area, triple phase boundary (TPB) length, and the structural tortuosity factors based on the three dimensional structure obtained by the FIB-SEM. Iwai *et al.* [58] evaluated the triple-phase boundary density and tortuosity factor based on Ni-YSZ microstructure reconstructed by the FIB-SEM. Suzue *et al.* [59] have conducted the three dimensional lattice Boltzmann method (LBM) simulation to assess the performance of SOFC anode. Shikazono *et al.* [62] used the three dimensional lattice Boltzmann method to solve the transport equations and the electrochemical reactions. Matsuzaki *et al.* [26] predicted the overpotential based on the microstructures obtained by the FIB-SEM. Kim [27] experimentally tested LSCF-GDC composite cathodes with different LSCF/GDC volume ratios, and reconstructed three-dimensional microstructures of these cathodes by the FIB-SEM.

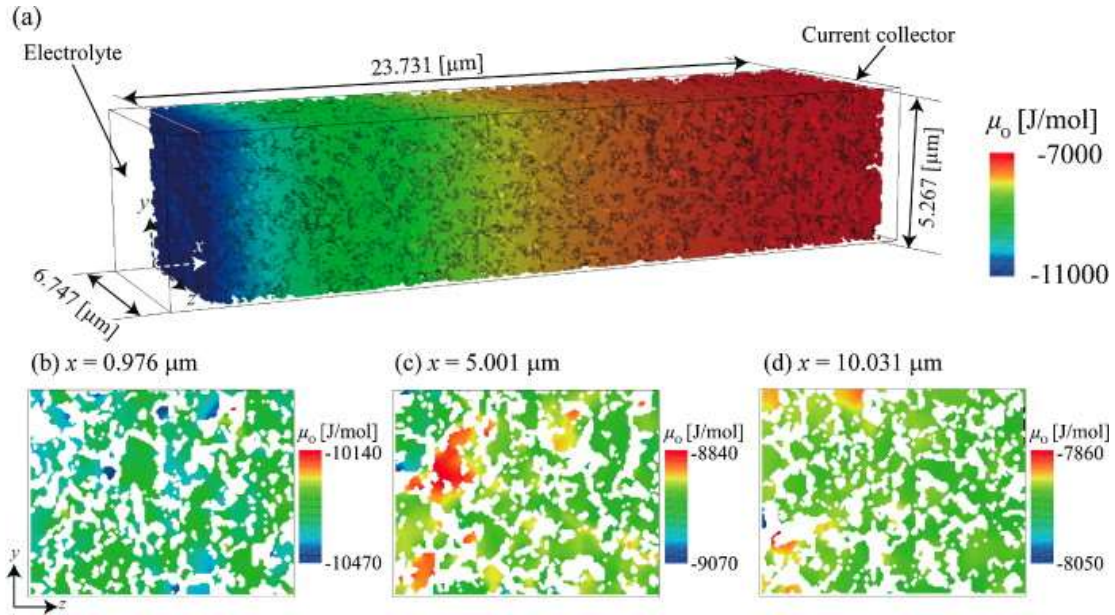


Fig. 1-12 Oxygen chemical potential μ_o distribution in pure LSCF cathode at $T = 1023$ K, $O_2 = 20\%$, $i = 0.1$ A/cm². [26]

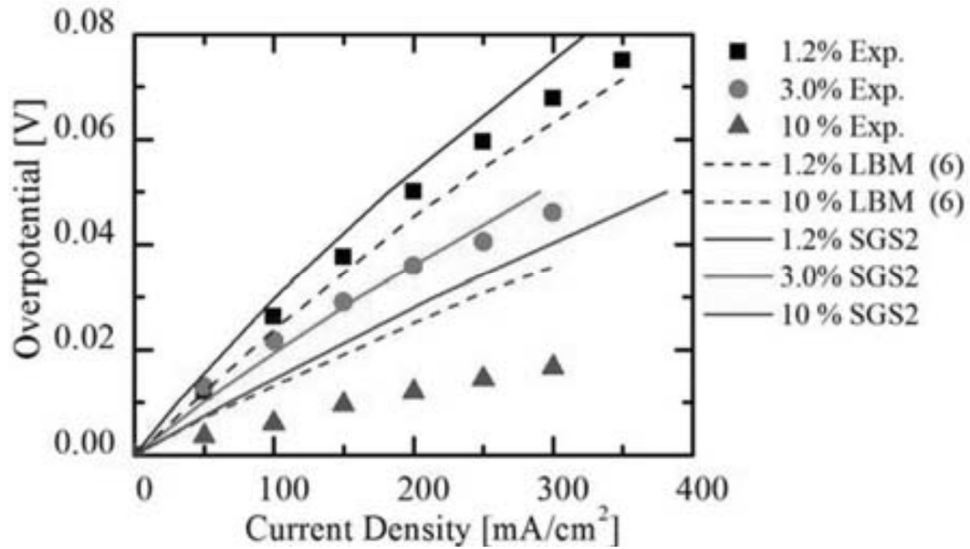


Fig. 1-13 LSCF cathode overpotential simulation results by different models compared with the experiment data [60].

1.6.2 Optimization methods

In order to give further guidance to SOFC design, the microstructures of the electrodes should be optimized to maximize the electrochemical performance.

Generally, the numerical optimizations can be divided into two categories, i.e. heuristic or non-heuristic optimizations [61]. During heuristic optimization, the representative cases are evaluated, and the optimal case is selected among these representative cases [27,49,61]. However, in order to obtain a fully optimal result, a huge number of representative cases are required to be computed [61]. Thus, common practice of the heuristic optimizations either bear a heavy computational load [49], or obtain a locally optimized result. For example, Bertei *et al.* applied heuristic optimization to obtain the optimal shape of the $Y_{0.08}Zr_{0.92}O_{1.96}$ (YSZ) pillars inside the Ni-YSZ anode. During optimization of Bertei *et al.*, in order to reduce the computational load, only limited cases of YSZ pillars are evaluated during simulation, and the simulation is conducted two-dimensionally, thus the structure is not fully optimized. What is more, many three-dimensional geometric details are lost during the simulation.

Non-heuristic optimizations involve evaluation of the gradient of the objective function, which requires less computational load to obtain a fully optimized result [61]. Adjoint method is one of the popular models for non-heuristic optimizations. Secanell *et al.* [62] used the adjoint method to optimize the Pt loading and porosity to maximize the cell current density in the proton exchange membrane fuel cell (PEMFC). Kapadia *et al.* [63] applied adjoint method to optimize the channel shape of the SOFC electrode.

Onishi *et al.* [64] introduced the adjoint method to obtain the optimal shape of the YSZ pillar to maximize the performance of the Ni-YSZ anode. In the optimization of Onishi *et al.*, 3D microstructure is considered, and the adjoint method enables a full optimization of the Ni-YSZ anode. During the simulation of Onishi *et al.*, the computational domain is divided into the electrode region and the electrolyte region. In the electrode region, electrode materials and pore phases are assumed to be homogeneously distributed. The electrolyte region is composed of dense electrolyte material with high ionic conductivity. And the electrochemical reaction is assumed to take place only at the electrode region. However, the electrochemical reaction also takes place at the electrode-electrolyte interface. The electrode-electrolyte interface reaction is expected to affect the optimization results. For instance, in pure LSCF cathode with GDC electrolyte, LSCF/GDC/pore TPB reaction takes place at the electrode-electrolyte

interface, and this interface TPB reaction is expected to influence the optimization result of GDC pillar inside the pure LSCF cathode.

1.7 Objectives of the present study

In the present study, the optimal 3D microstructure of pure porous LSCF cathode is obtained with the adjoint method. Then, the electrochemical performances of pure LSCF cathode and LSCF-GDC composite cathode are predicted with numerical simulations to estimate the electrochemical influence of the GDC pillar. Finally, the electrode-electrolyte interface structure are optimized using numerical optimization, and the characteristic of the optimized structure is discussed.

For the optimization of the microstructure of the pure porous LSCF cathode, the computational domain is composed of LSCF phase and pore phase. Only LSCF/pore double phase boundary (DPB) reaction which takes place at the LSCF-pore interface is considered. During numerical optimization, the LSCF microstructure is transformed until the total amount of reaction current density in the whole computational domain is maximized. Then, different initial structures are applied during optimization, and the characteristics of the optimal LSCF microstructures are discussed in terms of the optimized structural parameters and the electrochemical properties.

To estimate the electrochemical influence of the GDC pillars in the LSCF cathodes, 3D microstructure obtained with FIB-SEM is used during the numerical simulation. And then, further investigations of the electrochemical properties of the GDC pillars are carried out by examining the electrochemical influence of GDC pillars inserted inside the LSCF cathodes microstructures with various particle radii.

The optimization of the electrode-electrolyte interface is based on a computational domain which consists of electrode and electrolyte regions. In the electrode region, electrode and pore phases are assumed to be homogeneously distributed. The electrolyte region is composed of the dense electrolyte phase with high ionic conductivity. Electrochemical reactions are assumed to take place at both the

Chapter 3

Effects of Micro GDC pillars in Pure LSCF and LSCF-GDC Composite Cathode

3.1 Experiment

3.1.1 Fabrication of samples

The detailed fabrication procedure of samples are introduced in Ref. [27]. GDC powder (Shin-etsu Chemical Corporation) is pressed to fabricate the electrolyte pellet, which is followed by 5-hour sintering under 1550 °C. As for the SOFC cathode composed of pure LSCF, the commercial LSCF (Fuel Cell Materials Corporation) is screen-printed onto the surface of the electrolyte which is followed by one-hour sintering under 1150 °C. For the SOFC cathode composed of LSCF-GDC composite, we mixed the LSCF and GDC powders with 1:1 volume ratio, and the mixture is screen-printed onto the surface of the electrolyte which is followed by one-hour sintering under 1150 °C.

3.1.2 Observation with FIB-SEM

The pure LSCF cathode and the LSCF-GDC cathode three-dimensional microstructures are obtained by the technique of FIB-SEM (NVision 40, Carl Zeiss); a sequent of SEM images with a pixel size of 26 nm at an interval of 50 nm is obtained.

LSCF, GDC and pore phases in the 3D microstructures are distinguished according to the gray scales of the SEM images [27,28]. In order to facilitate the 3D electrochemical simulation, the 3D structure acquired from the FIB-SEM is re-structures with a voxel size of 100 nm. During the re-structuring procedure, each coarser voxel is represented by the phase which has largest volume fraction [26].

3.1.3 Shrinking the particle sizes of microstructures

The cathode thicknesses of the microstructures are mirror-extended into 25 μm to ensure that the samples used in simulation is the same as the thickness applied during experiment, which is shown in Fig. 3-1.

According to Section 2, small particle size is preferred to maximize the electrochemical performance of LSCF cathode. In order to investigate that how the GDC pillars influence the performance of the microstructure with small particle sizes, the 3D microstructures are shrunk for ten times than the original FIB-SEM structure, and the structures are also extended into the cathode thickness of $25\ \mu\text{m}$ to maintain the thickness the same as the experiment operation.

Table 3-1 shows the structural parameters of the 3D microstructures. The double phase boundary of LSCF/pore is computed with marching-cubes (MC) method [66]. In MC method, the geometry of the eight neighboring voxels can be represented by the patterns as shown in Fig. 3-4 (a). The surface areas are computed by summing up all the surface according to specific patterns. A TPB segment is defined if the edge of a voxel is surrounded by three different phases. As shown in Fig. 3-4 (b), the centroid method is applied to obtain the triple phase boundary of LSCF/GDC/pore [68].

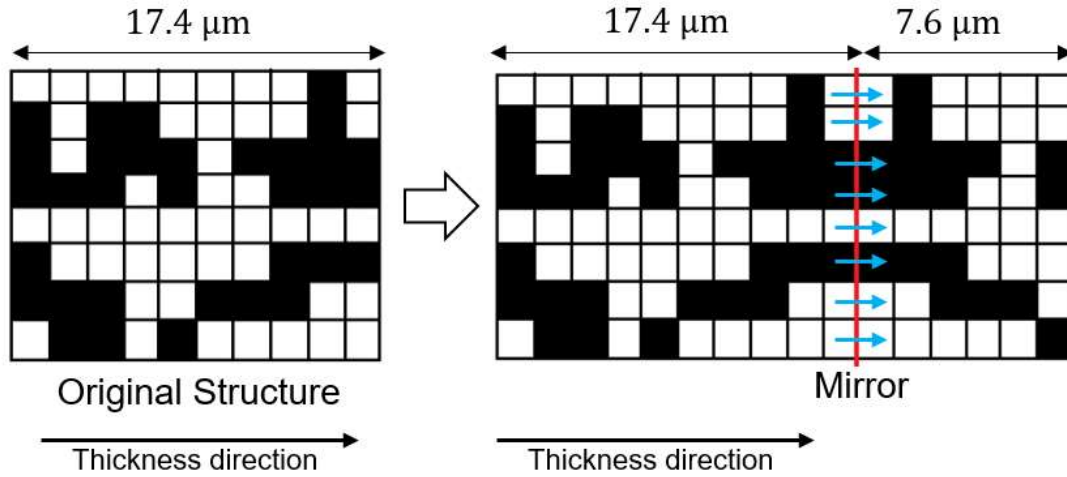


Fig. 3-1. Scheme of mirror symmetric extension. [84]

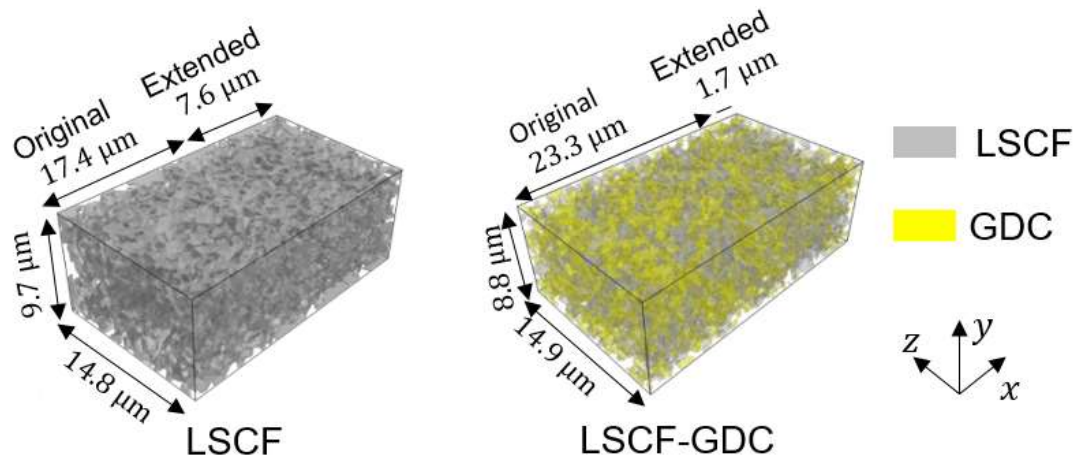


Fig. 3-2 Three-dimensional microstructures of pure LSCF and LSCF-GDC composite cathodes. [84]

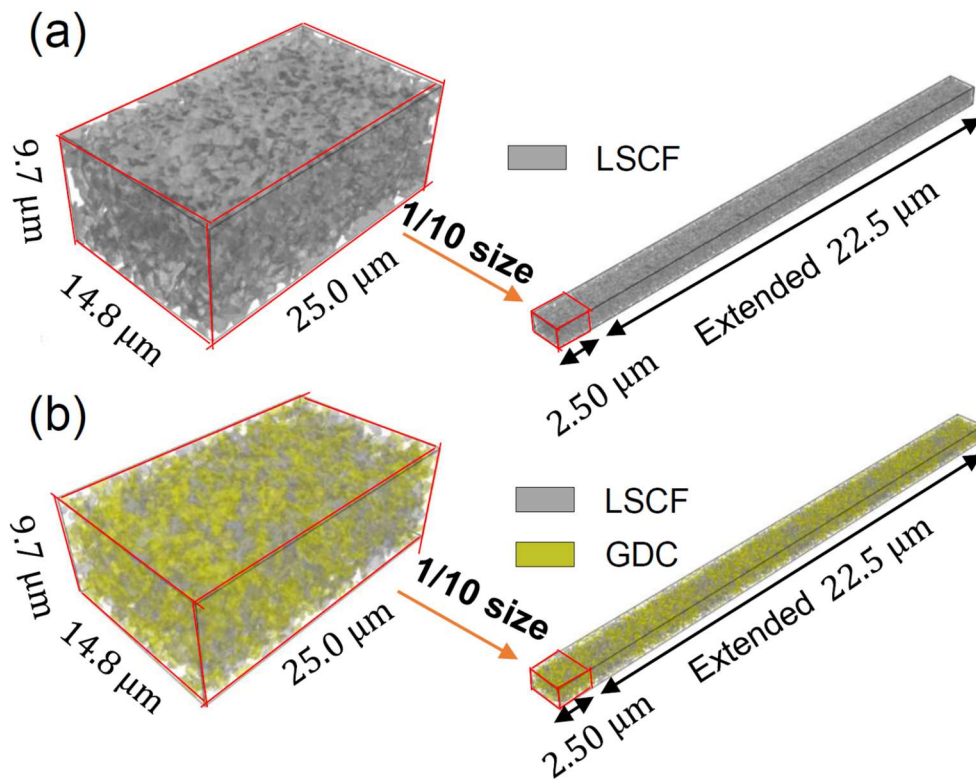


Fig. 3-3 Microstructures with 1/10 size. (a) Pure LSCF and (b) LSCF-GDC cathodes. [84]

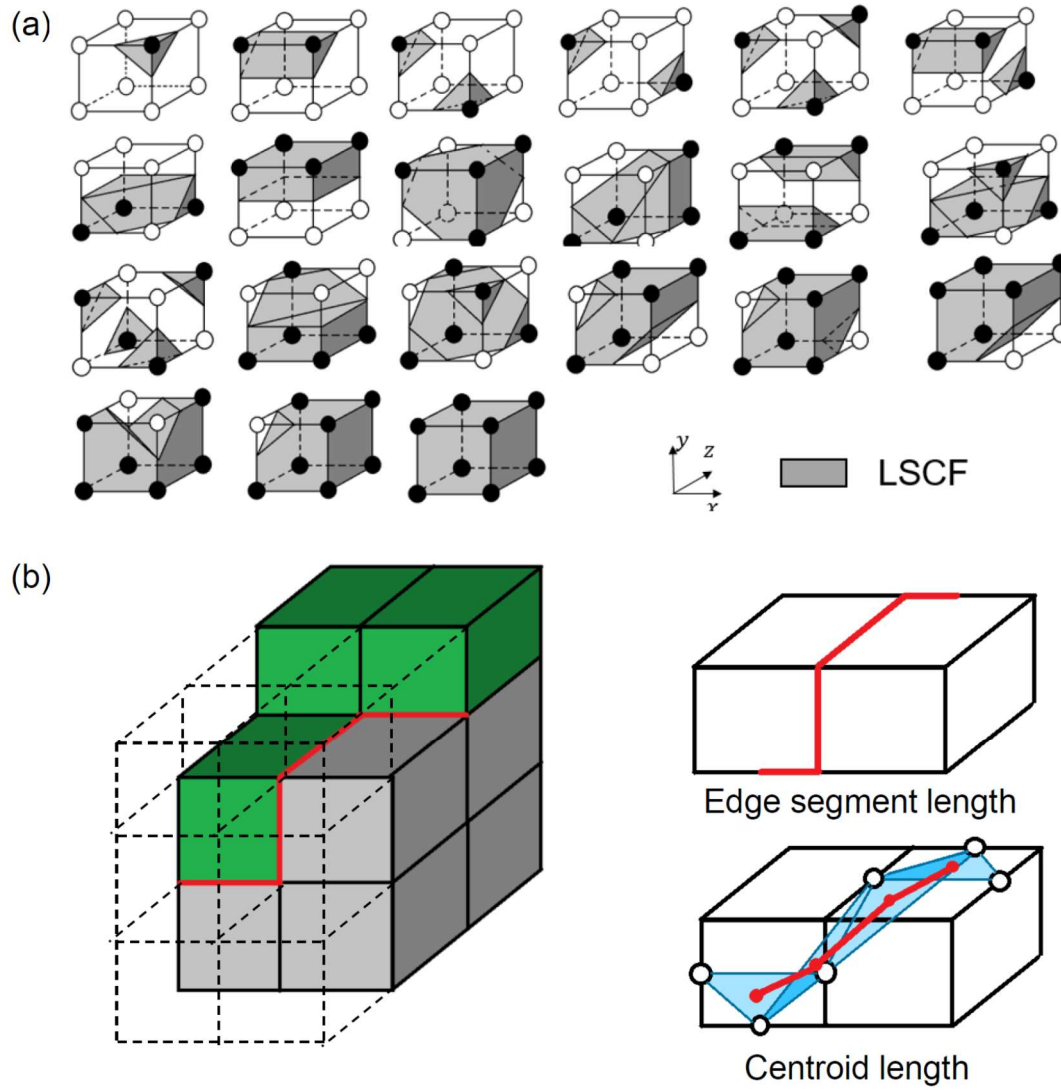


Fig. 3-4 Schemes of calculating (a) DPB area by the marching cubes method, and (b) TPB length by the centroid method. [84]

Table 3-1 Particle radii, DPB densities and TPB densities of different cathode microstructures [84]

Parameters		Pure LSCF	LSCF-GDC
Original sized microstructure	Pore radius (μm)	0.277	0.459
	LSCF particle radius (μm)	0.463	0.326
	GDC particle radius (μm)	-	0.305
	LSCF/pore DPB area density ($\mu\text{m}^2/\mu\text{m}^3$)	1.934	0.9887
	LSCF/GDC/pore TPB length density ($\mu\text{m}/\mu\text{m}^3$)	-	3.377
1/10 sized microstructure	Pore radius (μm)	0.0277	0.0459
	LSCF particle radius (μm)	0.0463	0.0326
	GDC particle radius (μm)	-	0.0305
	LSCF/pore DPB area density ($\mu\text{m}^2/\mu\text{m}^3$)	19.34	9.887
	LSCF/GDC/pore TPB length density ($\mu\text{m}/\mu\text{m}^3$)	-	337.7

3.1.4 Reconstruction of the microstructures with GDC pillars

As shown in Figs. 3-5 and 3-6, GDC pillar structure replaces the volumes of the 3D microstructures. In Fig. 3-5, the width of the pillars is maintained at 7 μm , In Fig. 3-6, the width of the pillars is maintained at 0.7 μm . The length of the pillars is varied in order to investigate the electrochemical effects of pillars.

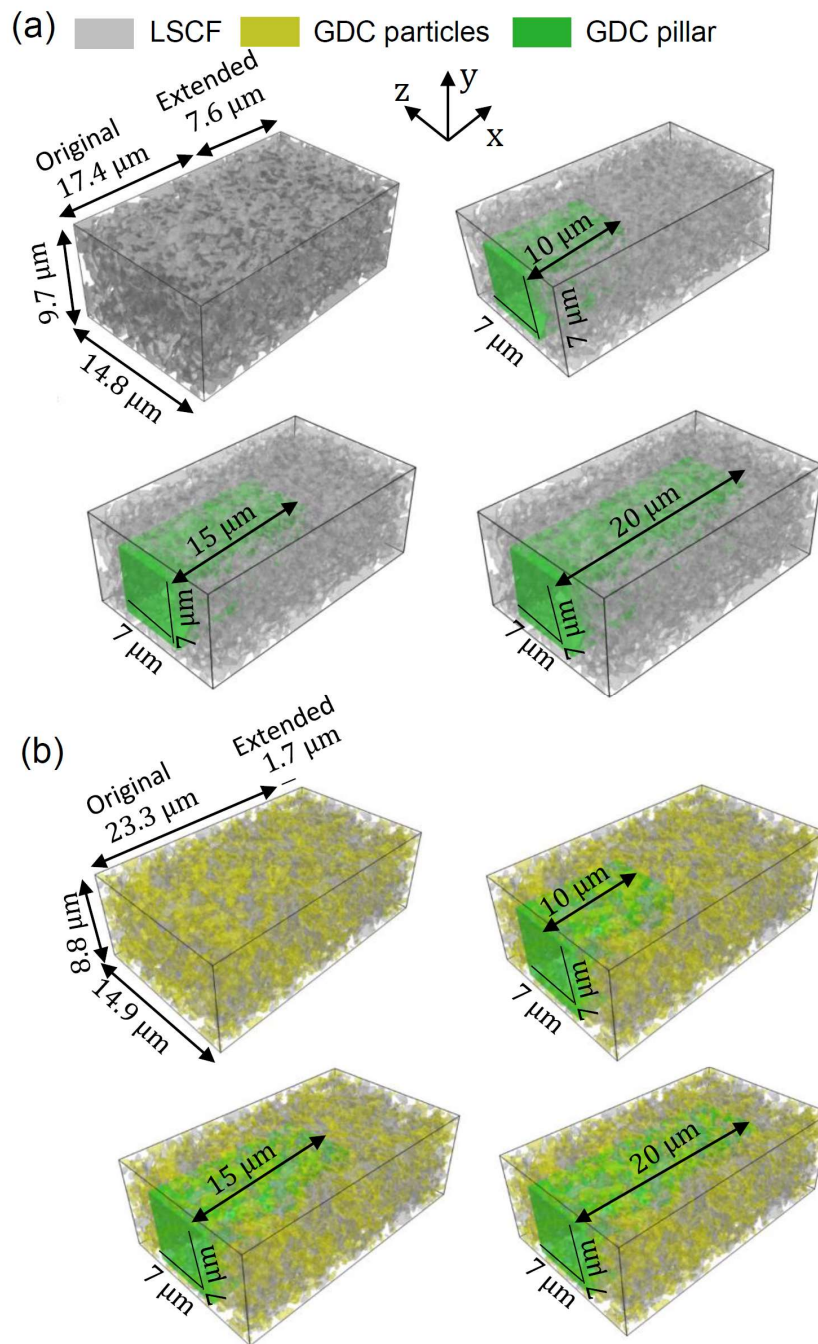


Fig. 3-5 Original sized (a) pure LSCF cathode with GDC pillars and (b) LSCF-GDC composite cathode with GDC pillars. [84]

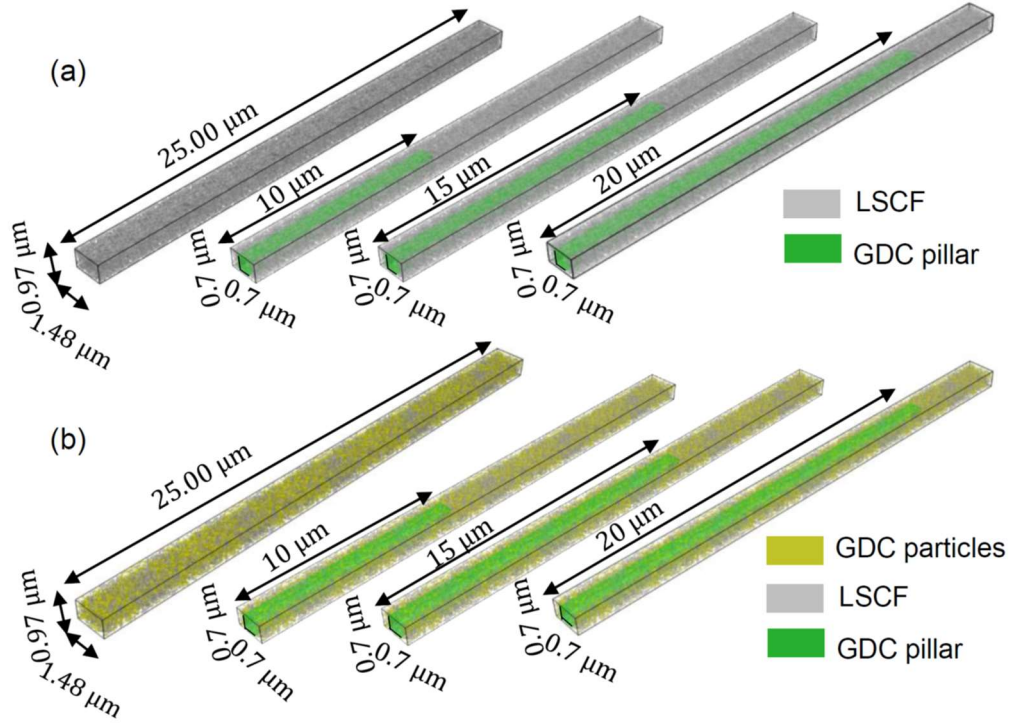


Fig. 3-6 1/10 sized (a) pure LSCF cathode with GDC pillars and (b) LSCF-GDC composite cathode with GDC pillars. [84]

3.2 Numerical simulation

3.2.1 Electron and ion transport equations

In the present study, the LSCF is assumed to be mixed ionic and electronic conductive (MIEC), and the GDC is assumed to be only ionic conductive. The electron and ion transport equations is shown as follows [26]:

$$\nabla \frac{\sigma_{e^-}}{F} \nabla \tilde{\mu}_{e^-} = i_{\text{reac}} , \quad (3-1)$$

$$\nabla \frac{\sigma_{O^{2-}}}{2F} \nabla \tilde{\mu}_{O^{2-}} = -i_{\text{reac}}, \quad (3-2)$$

The electron and oxide ionic conductivities for LSCF are obtained from Refs. [26,69], and the ionic conductivity of GDC are obtained from Ref. [70].

$$\log_{10}\sigma_{e^-,LSCF} = -0.0095(\log_{10}p_{O_2})^2 - 0.0011 \cdot \log_{10}p_{O_2} + 4.8152, \quad (3-3)$$

$$\sigma_{O^{2-},LSCF} = D_v \left(\frac{1}{2} \frac{\partial \delta}{\ln \partial \delta} \right) \left(\frac{8F^2}{RTV_{mol}} \right), \quad (3-4)$$

$$\sigma_{O^{2-},GDC} T = 1.09 \times 10^7 \exp\left(\frac{0.64/eV}{RT}\right), \quad (3-5)$$

where δ is defined as oxide nonstoichiometry [71], D_v is defined as diffusion coefficient of structure vacancy [72], $V_{mol} = 35.17 \times 10^{-6} \text{ m}^3/\text{mol}$ [73].

3.2.2 Gas transport equation

Convection is ignore in the current study [68], we apply the dusty gas model (DGM) to obtain the diffusivity with assuming the total pressure is constant [74].

$$\frac{N_i}{D_{i,k}} + \sum_{j=1, j \neq i}^n \frac{x_j N_i - x_i N_j}{D_{i,j}} = -\frac{1}{RT} \nabla P_i, \quad (3-6)$$

Where the subscript i is the gas species i , x is the molar fraction, N represents the mole flux, P represents the gas partial pressure, $D_{i,k}$ is the coefficient of the Knudsen diffusion, $D_{i,j}$ is the coefficient of the binary diffusion. Subscripts i and j are the species of gas. Eq. (3-6) can be transformed into:

$$N_{O_2} = -\left(\frac{1-\alpha x_{O_2}}{D_{O_2 N_2}} + \frac{1}{D_{O_2, k}}\right)^{-1} \nabla C_{O_2}, \quad (3-7)$$

where C represents the concentration, α is obtained from the Graham's law [26]. Binary diffusion coefficient $D_{O_2 N_2}$, Knudsen diffusion coefficient $D_{O_2, k}$, and α are

obtained as:

$$D_{O_2N_2} = 0.01833 \sqrt{\frac{1}{M_{O_2}} + \frac{1}{M_{N_2}} \frac{T^{3/2}}{P\Omega_D \zeta_{O_2N_2}^2}} , \quad (3-8)$$

$$D_{O_2k} = 0.01833 \sqrt{\frac{8RT}{\pi M_{O_2}}} r , \quad (3-9)$$

$$\alpha = 1 - \sqrt{\frac{M_{O_2}}{M_{N_2}}} , \quad (3-10)$$

where r is the particle radius, Ω_D and $\zeta_{O_2N_2}$ are obtained as:

$$\Omega_D = 1.1336 \left(\frac{T}{\varepsilon}\right)^{-0.1814} , \quad (3-11)$$

$$\zeta_{O_2N_2} = (\zeta_{O_2} + \zeta_{N_2})/2, \quad (3-12)$$

$$\varepsilon/k = \sqrt{\varepsilon_{O_2} \cdot \varepsilon_{N_2}}/k, \quad (3-13)$$

where $\zeta_{O_2} = 3.54 \text{ \AA}$, $\zeta_{N_2} = 3.68 \text{ \AA}$, $\frac{\varepsilon_{O_2}}{k} = 88.0 \text{ K}$, $\frac{\varepsilon_{N_2}}{k} = 91.5 \text{ K}$.

According to Eq. (3-7), D_{O_2} is computed as:

$$D_{O_2} = \left(\frac{1-\alpha x_{O_2}}{D_{O_2N_2}} + \frac{1}{D_{O_2,k}}\right)^{-1}, \quad (3-14)$$

The gas transport governing equation can be transformed as:

$$\nabla[D_{O_2} \cdot \nabla C_{O_2}] = -\frac{1}{4F} i_{\text{reac}}, \quad (3-15)$$

3.2.3 Electrochemical reactions

In the present study, the LSCF/pore DPB and LSCF/GDC/pore TPB reactions are computed as follows [27]:

$$i_{\text{reac,TPB}} = i_{0,\text{TPB}} L_{\text{TPB}} \left\{ \exp\left(\frac{2.0F}{RT} \eta_{\text{act}}\right) - \exp\left(-\frac{2.0F}{RT} \eta_{\text{act}}\right) \right\}, \quad (3-16)$$

$$i_{\text{reac,DPB}} = i_{0,\text{DPB}} A_{\text{DPB}} \left\{ \exp\left(\frac{1.2F}{RT} \eta_{\text{act}}\right) - \exp\left(-\frac{1.0F}{RT} \eta_{\text{act}}\right) \right\}, \quad (3-17)$$

where L_{TPB} and A_{DPB} are the TPB and DPB densities. While exchange current densities are obtained as: $i_{0,\text{DPB}} = 40.99 \text{ A/m}^2$ and $i_{0,\text{TPB}} = 7.9533 \times 10^{-6} \text{ A/m}$.

The η_{act} is expressed as [26]:

$$\eta_{\text{act}} = -\frac{1}{2F} (2\tilde{\mu}_{\text{e}^-} - \tilde{\mu}_{\text{O}^{2-}} + [\frac{1}{2}RT \log p_{\text{O}_2, \text{gas}}]_{\text{RE}}), \quad (3-18)$$

Cathode overpotential η_{cathode} is expressed by the following equation [26]:

$$\begin{aligned} \eta_{\text{cathode}} &= E_{\text{Nernst}} - (E_{\text{CC/S}} - E_{\text{RE/S}}) - \eta_{\text{ohm,CC}} - \eta_{\text{ohm,lyte}} - \eta_{\text{ohm,RE}} \quad (3-19) \\ &= \frac{RT}{4F} \log\left(\frac{p_{\text{O}_2, \text{CC}}}{p_{\text{O}_2, \text{RE}}}\right) - \frac{1}{F} (\tilde{\mu}_{\text{e}^-, \text{RE/S}} - \tilde{\mu}_{\text{e}^-, \text{CC/S}}) - \frac{1}{F} (\tilde{\mu}_{\text{e}^-, \text{CC/S}} - \tilde{\mu}_{\text{e}^-, \text{cathode/CC}}) - \\ &\quad \frac{1}{2F} (\tilde{\mu}_{\text{O}^{2-}, \text{cathode/lyte}} - \tilde{\mu}_{\text{O}^{2-}, \text{lyte/RE}}) - \frac{1}{F} (\tilde{\mu}_{\text{e}^-, \text{lyte/RE}} - \tilde{\mu}_{\text{e}^-, \text{RE/S}}) \\ &= \frac{RT}{4F} \log\left(\frac{p_{\text{O}_2, \text{CC}}}{p_{\text{O}_2, \text{RE}}}\right) - \frac{1}{2F} \{ \tilde{\mu}_{\text{O}^{2-}, \text{cathode/lyte}} - 2\tilde{\mu}_{\text{e}^-, \text{cathode/cc}} - \mu_{\text{O}, \text{lyte/RE}} \} \\ &= -\frac{1}{2F} \{ \tilde{\mu}_{\text{O}^{2-}, \text{cathode/lyte}} - 2\tilde{\mu}_{\text{e}^-, \text{cathode/cc}} - \mu_{\text{O}}^0 - \frac{1}{2}RT \log p_{\text{O}_2, \text{cc}} \} \quad . \end{aligned}$$

In addition, in y and z directions, adiabatic boundary conditions are applied. At the current collector side, constant gas composition (Dirichlet Boundary) is kept. At the both the current collector side and the electrolyte side, we use the Neumann boundary for electron and oxide ion transport, and constant flux of electron and oxide ion are maintained.

3.2.4 LBM model

Lattice Boltzmann method (LBM) [76] is used for solving solve Eqs. (3-1), (3-2), and (3-15), which is given as:

$$f_i(x + c_i\Delta t, t + \Delta t) = f_i(x, t) - \frac{1}{t^*(x, t)} [f_i(x, t) - f_i^{eq}(x, t)] + w_i\Delta t, \quad (3-20)$$

where f_i is the functions of potential density distribution, f_i^{eq} is expressed by following equation:

$$f_i^{eq} = \frac{1}{6} \sum_{i=1}^6 f_i(x, t), \quad (3-21)$$

The relaxation time t^* is expressed as:

$$t^*(x, t) = 0.5 + \frac{3D(x, t)\Delta t}{\Delta x^2}, \quad (3-22)$$

At the boundaries, halfway bounce-back scheme is applied:

$$f_i(x + c_i\Delta t, t + \Delta t) = f_i(x + c_i\Delta t, t + \Delta t), \quad (3-23)$$

3.2.5 Validation

The measured overpotentials of the pure LSCF and LSCF-GDC composite cathodes with the same microstructure as Fig. 3-2 are reported in Kim et al. [27]. Figures 3-7 and 3-8 show the comparison of the measured overpotential and the predicted overpotentials by different models under 700 °C, pure oxygen, and current density of $i = 0.05$ A/cm². As shown in the electrochemical results, the computational error with grid sizes of 50 nm and 100 nm are less than 10%; while the computational error with grid size of 200 nm is over 20% for LSCF-GDC composite cathode, under 500 A/m². In order to ensure the computational accuracy and relieve the computational load, 100 nm grid size is used for original sized microstructures in the present study.

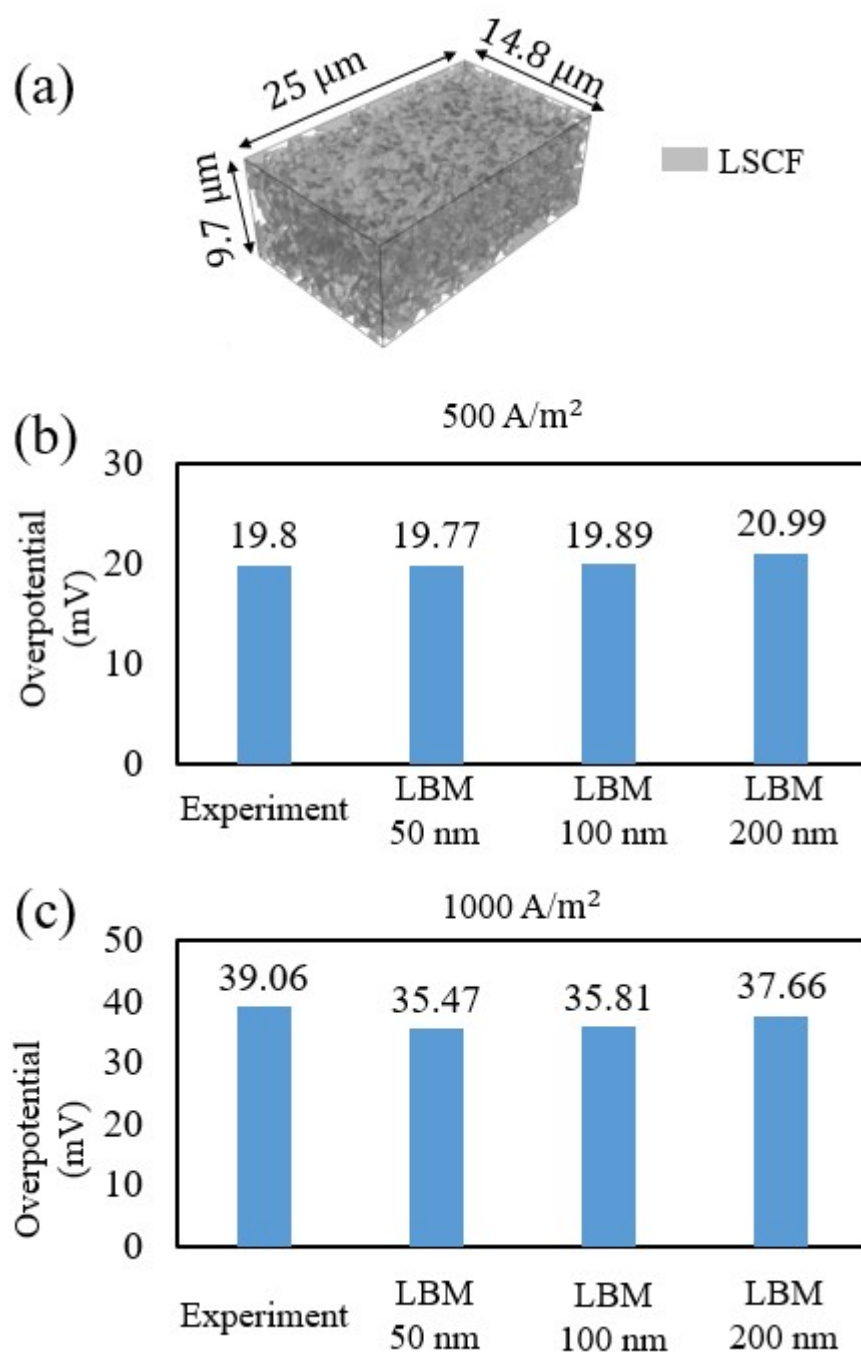


Fig. 3-7 (a) 3D microstructure of pure LSCF cathode, (b) electrochemical results under current density of 500 A/m^2 , and (c) electrochemical results under current density of 1000 A/m^2 . [84]

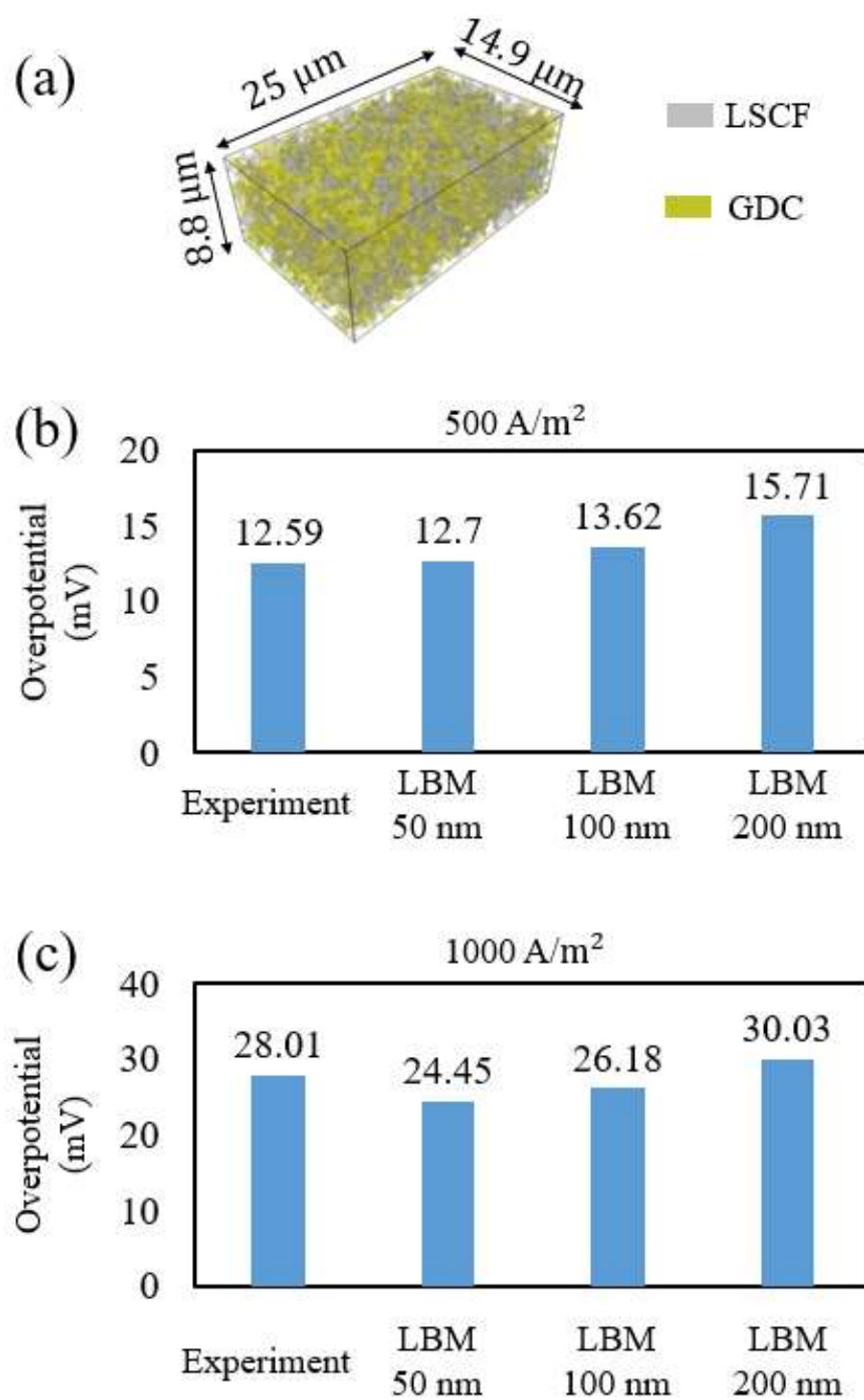


Fig. 3-8 (a) 3D microstructure of LSCF-GDC cathode, (b) electrochemical results under current density of 500 A/m^2 , and (c) electrochemical results under current density of 1000 A/m^2 . [84]

3.3 Computational results

3.3.1 Effects of cathode composition and particle size

The simulation in this section is based on the condition of $T = 700\text{ }^{\circ}\text{C}$, $i = 500\text{ A/m}^2$ and pure oxygen. From the simulation results in Fig. 3-11, the LSCF-GDC cathode improves the electrochemical performance comparing with pure LSCF cathode. It is because the LSCF-GDC composite cathode increases the cathode effective conductivities and TPB densities. What is more, shrinking of the particle sizes improves the cathode performance. This is attributed to that TPB and DPB densities improve a lot for smaller particle radii. This phenomenon is also demonstrated for the reactive thickness shown in Fig. 3-13 (b) and Fig. 3-12.

It is observed from Fig. 3-11 that the LSCF-GDC reduces the overpotential more significantly for smaller particle radii. As implied at Table 3-2, when the 3D structure is shrunk into 1/10 of the original structure size, the LSCF/pore DPB density improves ten times than the original, while the LSCF/GDC/pore TPB density improves for one hundred times. Therefore, it is concluded that the shrinking the particle size improve the LSCF/GDC/pore TPB more obviously than the LSCF/pore DPB density.

Figure 3-9 shows that the oxygen partial pressure is maintained as constant in the pore phase, this is attributed to the low current densities and thin cathode thickness is applied in the current study, which is also consistent with Ref. [26,77]. On the other hand, according to Fig. 3-10, the chemical potential of the oxygen along the thickness direction has an increasing gradient. This is attributed to that the region near the electrolyte is characterized with more electrochemical reactions.

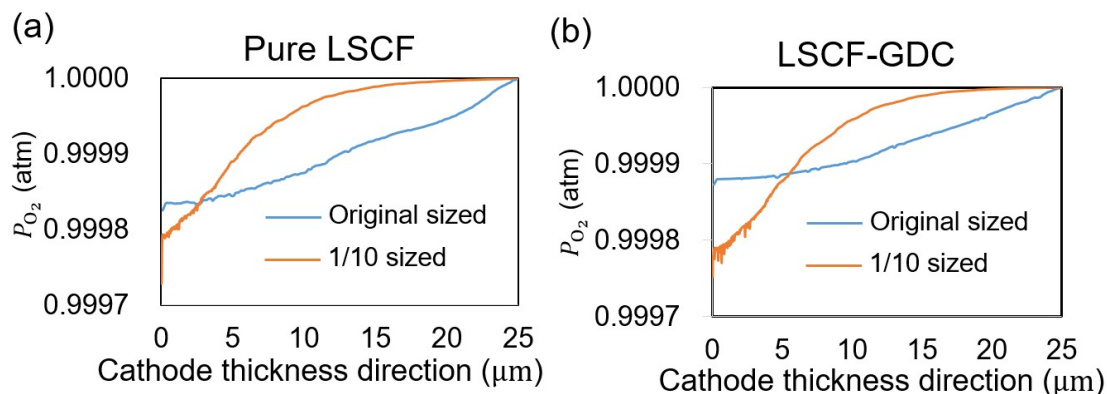


Fig. 3-9 Averaged oxygen pressures at each cross-section in the gas phase of (a) pure LSCF and (b) LSCF-GDC composite cathodes. [84]

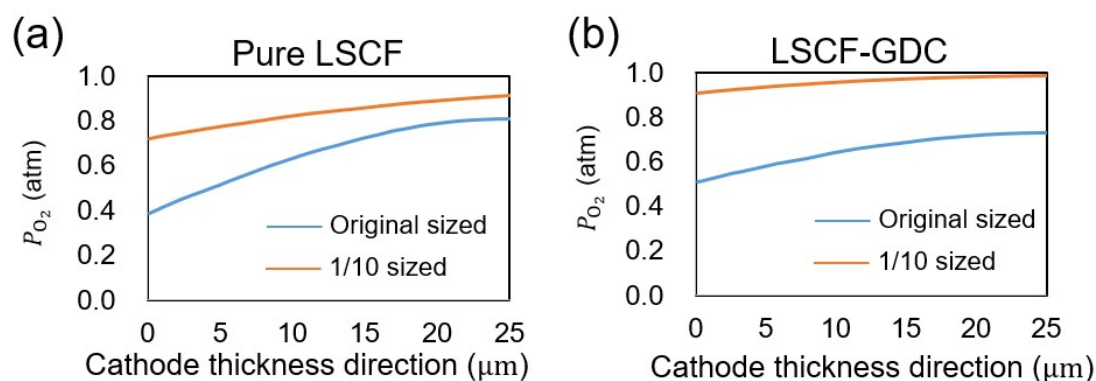


Fig. 3-10 Averaged oxygen pressures at each cross-section in the solid phase of (a) pure LSCF and (b) LSCF-GDC composite cathodes. [84]

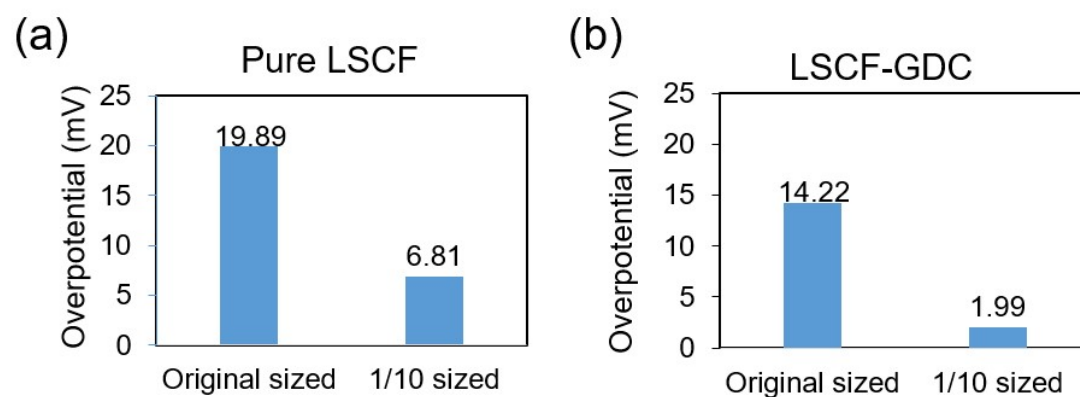


Fig. 3-11 Predicted overpotentials of (a) pure LSCF and (b) LSCF-GDC composite cathodes. [84]

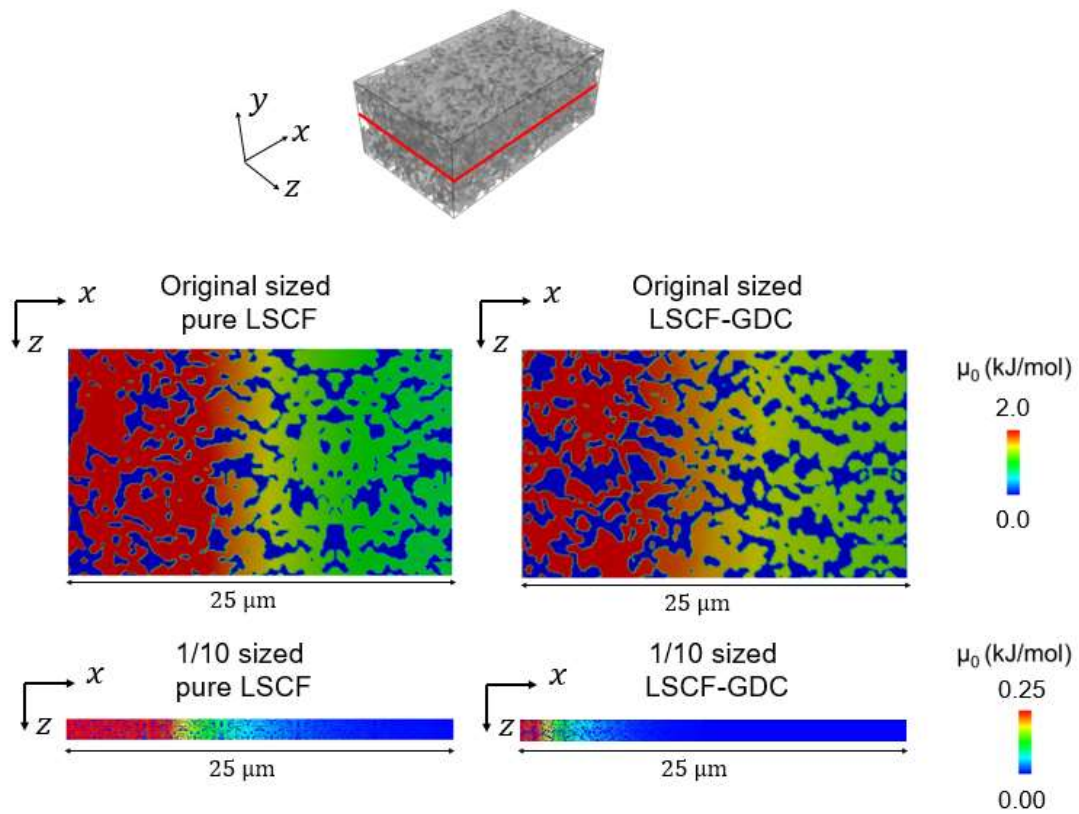


Fig. 3-12 Oxygen ion electrochemical potential distributions of the pure LSCF and LSCF-GDC composite cathodes with different particle size. [84]

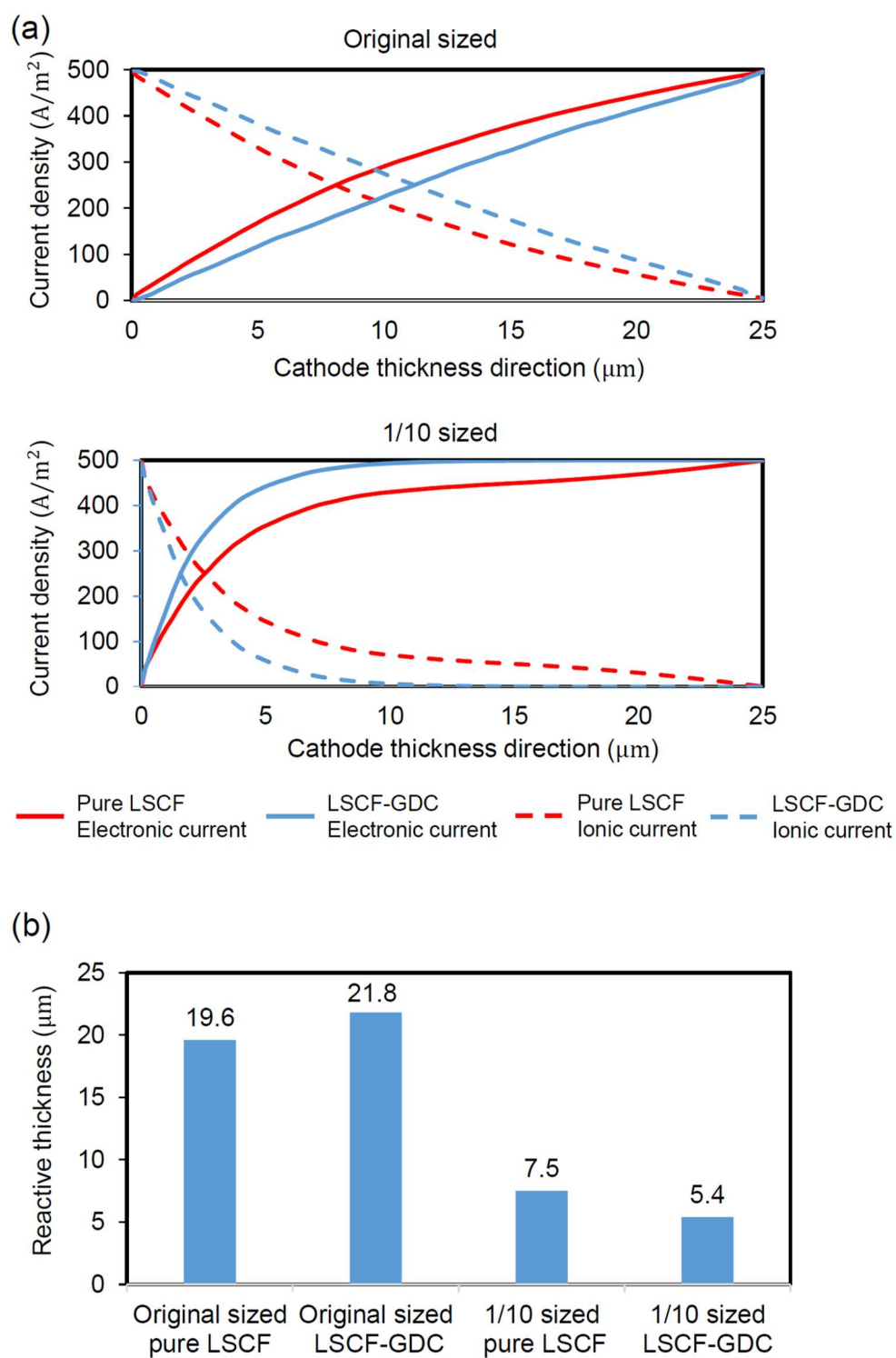


Fig. 3-13 (a) Electronic and ionic current density distributions and (b) reactive thicknesses of different microstructures. [84]

3.3.2 Effect of GDC pillars on electrochemical performance

According to the overpotential in Fig. 3-16, the GDC pillar improves the electrochemical performance of LSCF cathode. This is because the GDC pillars with high ionic conductivity greatly expand the reactive regions as shown in Fig. 3-15. What is more, according to Figs. 3-17 and 3-18, for the microstructure which has no pillars, the oxygen ion potential is concentrated near the electrolyte side. However, for the structure with GDC pillars, the oxygen ion potential distribution is greatly extended.

It is also concluded from Fig. 3-16 that the GDC pillars can more effectively enhance the cell performance for pure LSCF than in LSCF-GDC cathode. This phenomenon is attributed to that the LSCF-GDC composite cathode is characterized with much higher cathode ionic conductivity than LSCF cathode, as shown in Table 3-2.

According to Fig. 3-16, when GDC pillar is longer, the performance improvement thanks to the GDC pillars is suppressed. When the length of GDC pillar is large enough, the enhancement of the effective ion conductivity gets small which is indicated in Table 3-2. What is more, longer pillar replaces the electrode region which was originally characterized with reaction. In addition, for the LSCF-GDC cathode, the initially connected LSCF region becomes isolated because of the GDC pillar, which has negative effect on the cell performance.

From Fig. 3-16, it is concluded that the improvement of the performance by the insertion of pillar structure is more obvious for 1/10 sized structures. This is because the reactive regions of the 1/10 sized structure are thin, therefore, the extension of reactive thickness is more pronounced for 1/10 sized structure as shown in Fig. 3-17.

Chapter 5

Conclusions

In the present study, the optimal 3D microstructure of pure porous LSCF cathode is obtained with the adjoint method. And then, the electrochemical performances of LSCF-GDC composite cathode microstructures are numerically simulated in order to clarify the effects of the GDC pillar. After that, the electrode-electrolyte interface structures are optimized using numerical optimization, and the characteristic of the optimized structure is discussed. Following conclusions are obtained:

1. The numerical model to optimize the porous LSCF microstructure is constructed, and the following conclusions are obtained according to the optimization:
 - The optimized cathode area specific resistance is largely reduced comparing with the structure obtained with FIB-SEM. The particle size is largely reduced during optimization, and the optimized LSCF volume fraction has a decreasing gradient along the cathode thickness direction.
 - The LSCF microstructure is optimized into porous LSCF even starting from different initial conditions which are completely different from the porous microstructure. The optimized structure starting from the FIB-SEM porous microstructure has better electrochemical performance. However, the optimized performance difference is not pronounced even with different initial structures.
 - The optimized LSCF volume fraction has a larger decreasing gradient along the thickness direction for larger TPB exchange current density.
2. The numerical simulation is carried out based on the three-dimensional microstructure reconstructed by FIB-SEM to investigate the effect of the GDC micro pillars. According to the numerical results for different microstructures, following conclusion can be drawn:
 - The GDC micro pillars improve the electrochemical performance by expanding the reactive regions. The performance improvement is more pronounced for small particles, because the GDC pillars can expand the reactive regions more effectively for the microstructures with smaller particle size.
 - The performance improvement is more pronounced for the pure LSCF cathode

than for the LSCF-GDC composite, because ionic conductivity is more effectively improved by the GDC pillars for the pure LSCF cathode.

- The performance improvement effect is suppressed if the GDC pillar is too long. This is because the GDC pillars replace the electrode region which is originally conductive.
3. The numerical model to optimize the electrode-electrolyte interface is constructed, and following conclusions are drawn:
- According to the optimization of the interface between the pure LSCF cathode and GDC electrolyte, the microstructure with optimized electrode-electrolyte interface has much better electrochemical performance than the microstructure with flat interface. The ASR of optimal microstructure is 2.88 times smaller than the original microstructure. In addition, the size of the optimized electrolyte region structure is independent from the computational domain and the initial microstructure shapes.
 - In order to give guidance to the microstructure design with various electrolyte materials and with various electrode microstructures, the influence of dimensionless numbers on the optimized microstructure is investigated. The change in the dimensionless parameter k is realized by changing $\sigma_{\text{O}^{2-}, \text{electrolyte}}$. The optimized electrolyte region size becomes smaller with larger $\sigma_{\text{O}^{2-}, \text{electrolyte}}$. The change in the dimensionless parameter $\Gamma_{\text{electrode}}$ is realized by changing the electrode region reaction coefficient, $\beta_{\text{electrode}}$. The reactive thickness of the electrode region becomes smaller with larger $\beta_{\text{electrode}}$, and the size of optimized electrolyte region size becomes smaller with larger $\beta_{\text{electrode}}$. The change in the dimensionless parameter $\Gamma_{\text{interface}}$ is realized by changing the interface reaction coefficient, $\beta_{\text{interface}}$. The area of the optimized electrode-electrolyte interface becomes larger with larger $\beta_{\text{interface}}$.

References

- [1] A. B. Stambouli, E. Traversa, Solid oxide fuel cells (SOFCs): A review of an environmentally clean and efficient source of energy, *Renew. Sustain. Energy Rev.* 6 (2002) 433–455. doi:10.1016/S1364-0321(02)00014-X.
- [2] G. Ang, Overcoming barriers to international investment in clean energy, 2015.
- [3] W. Young, H. Kumju, M. Seonaidh, J. O. Caroline, Sustainable consumption: green consumer behaviour when purchasing products, *Sustain. Dev. J.* 31 (2008) 20–31. doi:10.1177/0266242610391936.
- [4] <https://data.worldbank.org/indicator/EG.USE.COMM.FO.ZS>.
- [5] https://www.eia.gov/energyexplained/index.php?page=electricity_generating.
- [6] <https://ourworldindata.org/how-long-before-we-run-out-of-fossil-fuels>.
- [7] International Energy Agency. (2014). CO₂ Emissions From Fuel Combustion.
- [8] Intergovernmental Panel on Climate Change. (2007). Summary for policymakers.
- [9] Tsukimori, O. (2015). "Japan sets 26 percent cut in greenhouse gas emissions as target." *Reuters (2015 Jul 17th)*.
- [10] S. Fetter, (2009). How long will the world's uranium supplies last? *Scientific American (2009 Jan 24th)*.
- [11] <https://www.statista.com/statistics/265537/nuclear-energy-consumption-in-japan/>
- [12] G. M. Joselin Herbert, S. Iniyar, E. Sreevalsan, S. Rajapandian, A review of wind energy technologies, *Renew. Sustain. Energy Rev.* 11 (2007) 1117–1145. doi:10.1016/j.rser.2005.08.004.
- [13] D. Y. C. Leung, Y. Yang, Wind energy development and its environmental impact: A review, *Renew. Sustain. Energy Rev.* 16 (2012) 1031–1039. doi:10.1016/j.rser.2011.09.024.
- [14] G. K. Singh, Solar power generation by PV (photovoltaic) technology: A review, *Energy.* 53 (2013) 1–13. doi:10.1016/j.energy.2013.02.057.
- [15] V. Mehta, J. S. Cooper, Review and analysis of PEM fuel cell design and

- manufacturing, *J. Power Sources*. 114 (2003) 32–53. doi:10.1016/S0378-7753(02)00542-6.
- [16] I. Dincer, Renewable energy and sustainable development: a crucial review, *Renew. Sustain. Energy Rev.* 4 (2000) 157–175. doi:10.1016/S1364-0321(99)00011-8.
- [17] Y. Wang, K. S. Chen, J. Mishler, S. C. Cho, X.C. Adroher, A review of polymer electrolyte membrane fuel cells: Technology, applications, and needs on fundamental research, *Appl. Energy*. 88 (2011) 981–1007. doi:10.1016/j.apenergy.2010.09.030.
- [18] E. Antolini, The stability of molten carbonate fuel cell electrodes: A review of recent improvements, *Appl. Energy*. 88 (2011) 4274–4293. doi:10.1016/j.apenergy.2011.07.009.
- [19] G. J. K. Acres, Recent advances in fuel cell technology and its applications, *J. Power Sources*. 100 (2001) 60–66. doi:10.1016/S0378-7753(01)00883-7.
- [20] S. P. Jiang, S. H. Chan, A review of anode materials development in solid oxide fuel cells, *J. Mater. Sci.* 39 (2004) 4405–4439. doi:10.1023/B:JMSC.0000034135.52164.6b.
- [21] High temperature solid oxide fuel cell, (n.d.).
- [22] S. C. Paulson, V. I. Birss, Chromium Poisoning of LSM-YSZ SOFC Cathodes, *J. Electrochem. Soc.* 151 (2004) A1961. doi:10.1149/1.1806392.
- [23] P. Gannon, S. Sofie, M. Deibert, R. Smith, V. Gorokhovsky, Thin film YSZ coatings on functionally graded freeze cast NiO/YSZ SOFC anode supports, *J. Appl. Electrochem.* 39 (2009) 497–502. doi:10.1007/s10800-008-9682-4.
- [24] D. Kennouche, J. Hong, H. S. Noh, J. W. Son, S. A. Barnett, Three-dimensional microstructure of high-performance pulsed-laser deposited Ni-YSZ SOFC anodes, *Phys. Chem. Chem. Phys.* 16 (2014) 15249–15255. doi:10.1039/c4cp02251c.
- [25] T. Shimura, Z. Jiao, S. Hara, N. Shikazono, Quantitative analysis of solid oxide fuel cell anode microstructure change during redox cycles, *J. Power Sources*. 267 (2014) 58–68. doi:10.1016/j.jpowsour.2014.04.152.

- [26] K. Matsuzaki, N. Shikazono, N. Kasagi, Three-dimensional numerical analysis of mixed ionic and electronic conducting cathode reconstructed by focused ion beam scanning electron microscope, *J. Power Sources*. 196 (2011) 3073–3082. doi:10.1016/j.jpowsour.2010.11.142.
- [27] Y. T. Kim, Z. Jiao, N. Shikazono, Evaluation of $\text{La}_{0.6}\text{Sr}_{0.4}\text{Co}_{0.2}\text{Fe}_{0.8}\text{O}_{3-\delta}$ - $\text{Gd}_{0.1}\text{Ce}_{0.9}\text{O}_{1.95}$ composite cathode with three dimensional microstructure reconstruction, *J. Power Sources*. 342 (2017) 787–795. doi:10.1016/j.jpowsour.2016.12.113.
- [28] Y. T. Kim, N. Shikazono, Investigation of $\text{La}_{0.6}\text{Sr}_{0.4}\text{CoO}_{3-\delta}$ - $\text{Gd}_{0.1}\text{Ce}_{0.9}\text{O}_{2-\delta}$ composite cathodes with different volume ratios by three dimensional reconstruction, *Solid State Ionics*. 309 (2017) 77–85. doi:10.1016/j.ssi.2017.07.010.
- [29] C. H. Hua, C. C. Chou, Preparation of nanoscale composite LSCF/GDCS cathode materials by microwave sintering for intermediate-temperature SOFC applications, *Ceram. Int.* 41 (2015) S708–S712. doi:10.1016/j.ceramint.2015.03.128.
- [30] T. Carraro, J. Joos, B. Rüger, A. Weber, E. Ivers-Tiffée, 3D finite element model for reconstructed mixed-conducting cathodes: I. Performance quantification, *Electrochim. Acta*. 77 (2012) 315–323. doi:10.1016/j.electacta.2012.04.109.
- [31] W. Z. Zhu, S.C. Deevi, A review on the status of anode materials for solid oxide fuel cells, *Mater. Sci. Eng. A*. 362 (2003) 228–239. doi:10.1016/S0921-5093(03)00620-8.
- [32] S. Tao, J. T. S. Irvine, A redox-stable efficient anode for solid-oxide fuel cells, *Nat. Mater.* 2 (2003) 320–323. doi:10.1038/nmat871.
- [33] J. M. Haag, D. M. Bierschenk, S. A. Barnett, K. R. Poeppelmeier, Structural, chemical, and electrochemical characteristics of $\text{LaSr}_2\text{Fe}_2\text{CrO}_{9-\delta}$ -based solid oxide fuel cell anodes, *Solid State Ionics*. 212 (2012) 1–5. doi:10.1016/j.ssi.2012.01.037.
- [34] P. Addo, B. Molero-sanchez, A. Buyukaksoy, S. Paulson, V. Birss, C) (1-5). It has been suggested that H_2S inhibits the H_2 oxidation reaction (HOR) rates

- because it readily dissociates to form a surface adsorbed Ni-S layer (S, 66 (2015) 219–228.
- [35] H. He, Y. Huang, J.M. Vohs, R.J. Gorte, Characterization of YSZ-YST composites for SOFC anodes, *Solid State Ionics*. 175 (2004) 171–176. doi:10.1016/j.ssi.2004.09.033.
- [36] P. Gansor, K. Sabolsky, J. W. Zondlo, E.M. Sabolsky, Sr₂MgMoO_{6-δ}/Gd_{0.1}Ce_{0.9}O_{1.95} composite anode-supported solid oxide fuel cell (SOFC), *Mater. Lett.* 105 (2013) 80–83. doi:10.1016/j.matlet.2013.04.037.
- [37] S. P. Jiang, X. J. Chen, S. H. Chan, J. T. Kwok, GDC-Impregnated (La_{0.75}Sr_{0.25})(Cr_{0.5}Mn_{0.5})O₃ Anodes for Direct Utilization of Methane in Solid Oxide Fuel Cells, *J. Electrochem. Soc.* 153 (2006) A850. doi:10.1149/1.2179347.
- [38] J. Piao, K. Sun, N. Zhang, S. Xu, A study of process parameters of LSM and LSM-YSZ composite cathode films prepared by screen-printing, *J. Power Sources*. 175 (2008) 288–295. doi:10.1016/j.jpowsour.2007.09.078.
- [39] 金容兌, SOFCコンポジット空気極の微細構造および電極性能評価. 東京大学修士論文, 2014.
- [40] 金容兌, 固体酸化物形燃料電池コンポジット空気極の分極特性および電極微細構造に関する研究. 東京大学博士論文, 2014.
- [41] 大井彰洋, 固体酸化物形燃料電池LSCF-GDC空気極の三次元数値解析. 東京大学修士論文, 2015.
- [42] C. Sun, R. Hui, J. Roller, Cathode materials for solid oxide fuel cells: A review, *J. Solid State Electrochem.* 14 (2010) 1125–1144. doi:10.1007/s10008-009-0932-0.
- [43] Y. Leng, S. H. Chan, Q. Liu, Development of LSCF-GDC composite cathodes for low-temperature solid oxide fuel cells with thin film GDC electrolyte, *Int. J. Hydrogen Energy*. 33 (2008) 3808–3817. doi:10.1016/j.ijhydene.2008.04.034.
- [44] E. Perry Murray, M. J. Sever, S. A. Barnett, Electrochemical performance of (La, Sr)(Co, Fe)O₃–(Ce, Gd)O₃ composite cathodes, *Solid State Ionics*. 148 (2002)

- 27–34. doi:10.1016/S0167-2738(02)00102-9.
- [45] D. Klotz, J. Hayd, J. Szasz, N. H. Menzler, E. Ivers-Tiffée, Nano-Scaled Mixed Conductors for High Performance SOFCs at $\leq 600^{\circ}\text{C}$, *ECS Trans.* 61 (2014) 131. doi:<http://dx.doi.org/10.4236/ojo.2014.48035>.
- [46] K. Sato, C. Iwata, N. Kannari, H. Abe, Highly accelerated oxygen reduction reaction kinetics in colloidal-processing-derived nanostructured lanthanum strontium cobalt ferrite/gadolinium-doped ceria composite cathode for intermediate-temperature solid oxide fuel cells, *J. Power Sources.* 414 (2019) 502–508. doi:10.1016/j.jpowsour.2019.01.032.
- [47] K. Nagato, S. Shinagawa, N. Shikazono, S. Iwasaki, M. Nakao, SOFC Anode Based on YSZ Pillars, *ECS Trans.* 68 (2015) 1309–1314.
- [48] F. Delloro, M. Viviani, Simulation study about the geometry of electrode-electrolyte contact in a SOFC, *J. Electroceramics.* 29 (2012) 216–224. doi:10.1007/s10832-012-9766-8.
- [49] A. Bertei, F. Tariq, V. Yufit, E. Ruiz-Trejo, N. P. Brandon, Guidelines for the Rational Design and Engineering of 3D Manufactured Solid Oxide Fuel Cell Composite Electrodes, *J. Electrochem. Soc.* 164 (2017) F89–F98. doi:10.1149/2.0501702jes.
- [50] T. Okabe, Y. Kim, Z. Jiao, N. Shikazono, J. Taniguchi, Fabrication process for micropatterned ceramics via UV-nanoimprint lithography using UV-curable binder, *Jpn. J. Appl. Phys.* 57 (2018). doi:10.7567/JJAP.57.106501.
- [51] M. Zhi, S. Lee, N. Miller, N.H. Menzler, N. Wu, An intermediate-temperature solid oxide fuel cell with electrospun nanofiber cathode, *Energy Environ. Sci.* 5 (2012) 7066–7071. doi:10.1039/c2ee02619h.
- [52] C. Ding, T. Hashida, High performance anode-supported solid oxide fuel cell based on thin-film electrolyte and nanostructured cathode, *Energy Environ. Sci.* 3 (2010) 1729–1731. doi:10.1039/c0ee00255k.
- [53] A. S. Joshi, K. N. Grew, A. A. Peracchio, W.K.S. Chiu, Lattice Boltzmann modeling of 2D gas transport in a solid oxide fuel cell anode, *J. Power Sources.* 164 (2007) 631–638. doi:10.1016/j.jpowsour.2006.10.101.

-
- [54] Y. Komatsu, S. Kimijima, J. S. Szmyd, Numerical analysis on dynamic behavior of solid oxide fuel cell with power output control scheme, *J. Power Sources*. 223 (2013) 232–245. doi:10.1016/j.jpowsour.2012.09.048.
- [55] J. H. Nam, D. H. Jeon, A comprehensive micro-scale model for transport and reaction in intermediate temperature solid oxide fuel cells, *Electrochim. Acta*. 51 (2006) 3446–3460. doi:10.1016/j.electacta.2005.09.041.
- [56] J. R. Wilson, W. Kobsiriphat, R. Mendoza, H.-Y. Chen, J. M. Hiller, D. J. Miller, K. Thornton, P. W. Voorhees, S. B. Adler, S. A. Barnett, Three-dimensional reconstruction of a solid-oxide fuel-cell anode, *Nat. Mater.* 5 (2006) 541–544. doi:10.1038/nmat1668.
- [57] D. Gostovic, J. R. Smith, D. P. Kundinger, K. S. Jones, E. D. Wachsman, Three-Dimensional Reconstruction of Porous LSCF Cathodes, *Electrochem. Solid-State Lett.* 10 (2007) B214. doi:10.1149/1.2794672.
- [58] H. Iwai, N. Shikazono, T. Matsui, H. Teshima, M. Kishimoto, R. Kishida, D. Hayashi, K. Matsuzaki, D. Kanno, M. Saito, H. Muroyama, K. Eguchi, N. Kasagi, H. Yoshida, Quantification of SOFC anode microstructure based on dual beam FIB-SEM technique, *J. Power Sources*. 195 (2010) 955–961. doi:10.1016/j.jpowsour.2009.09.005.
- [59] Y. Suzue, N. Shikazono, N. Kasagi, Micro modeling of solid oxide fuel cell anode based on stochastic reconstruction, *J. Power Sources*. 184 (2008) 52–59. doi:10.1016/j.jpowsour.2008.06.029.
- [60] M. Kishimoto, H. Iwai, M. Saito, H. Yoshida, Three-Dimensional Simulation of SOFC Anode Polarization Characteristics Based on Sub-Grid Scale Modeling of Microstructure, *J. Electrochem. Soc.* 159 (2012) B315–B323. doi:10.1149/2.086203jes.
- [61] P. Andrei, G. Mixon, M. Mehta, V. Bevara, Design of the Catalyst Layers in PEMFCs Using an Adjoint Sensitivity Analysis Approach, *ECS Trans.* 66 (2015) 91–128. doi:10.1149/06608.0091ecst.
- [62] M. Secanell, R. Songprakorp, A. Suleman, N. Djilali, Multi-objective optimization of a polymer electrolyte fuel cell membrane electrode assembly,

- Energy Environ. Sci. 1 (2008) 378–388. doi:10.1039/b804654a.
- [63] S. Kapadia, W. K. Anderson, L. Elliott, C. Burdyslaw, Adjoint method for solid-oxide fuel cell simulations, J. Power Sources. 166 (2007) 376–385. doi:10.1016/j.jpowsour.2007.01.085.
- [64] J. Onishi, Y. Kametani, Y. Hasegawa, N. Shikazono, Development of a topology optimization method for electrolyte-electrode interfaces of solid oxide fuel cells based on the adjoint method, submitted to J. Power Sources, (2019).
- [65] V. Novák, F. Štěpánek, P. Kočí, M. Marek, M. Kubíček, Evaluation of local pore sizes and transport properties in porous catalysts, Chem. Eng. Sci. 65 (2010) 2352–2360. doi:10.1016/j.ces.2009.09.009.
- [66] G. M. Nielson, B. Hamann, The asymptotic decider: resolving the ambiguity in marching cubes, Proceeding Vis. '91. (1991) 83–91,. doi:10.1109/VISUAL.1991.175782.
- [67] B. Ahrenholz, J. Tölke, M. Krafczyk, Lattice-Boltzmann simulations in reconstructed parametrized porous media, Int. J. Comput. Fluid Dyn. 20 (2006) 369–377. doi:10.1080/10618560601024694.
- [68] N. Shikazono, D. Kanno, K. Matsuzaki, H. Teshima, S. Sumino, N. Kasagi, Numerical Assessment of SOFC Anode Polarization Based on Three-Dimensional Model Microstructure Reconstructed from FIB-SEM Images, J. Electrochem. Soc. 157 (2010) B665. doi:10.1149/1.3330568.
- [69] H. J. M. Bouwmeester, M. W. Den Otter, B. A. Boukamp, Oxygen transport in $\text{La}_{0.6}\text{Sr}_{0.4}\text{Co}_{1-y}\text{Fe}_y\text{O}_{3-\delta}$, J. Solid State Electrochem. 8 (2004) 599–605. doi:10.1007/s10008-003-0488-3.
- [70] S. B. C. H., Appraisal of Ce, Solid State Ionics. 129 (2000) 95–110.
- [71] H. Kudo, K. Yashiro, S. Hashimoto, K. Amezawa, T. Kawada, J. Mizusaki, Oxygen Transport in Perovskite Type Oxide $\text{La}_{0.6}\text{Sr}_{0.4}\text{Co}_{0.2}\text{Fe}_{0.8}\text{O}_{3-\delta}$, ECS Trans. 50 (2013) 37–42.
- [72] M. Kuhn, Y. Fukuda, S. Hashimoto, K. Sato, K. Yashiro, J. Mizusaki, Oxygen Nonstoichiometry and Thermo-Chemical Stability of Perovskite-Type $\text{La}_{0.6}\text{Sr}_{0.4}\text{Co}_{1-y}\text{Fe}_y\text{O}_{3-\delta}$ ($y = 0, 0.2, 0.4, 0.5, 0.6, 0.8, 1$) Materials, J. Electrochem. Soc.

- 160 (2013) F34–F42. doi:10.1149/2.050301jes.
- [73] K. Yashiro, I. Nakano, M. Kuhn, S. Hashimoto, K. Sato, J. Mizusaki, Electrical Conductivity and Oxygen Diffusivity of Perovskite-Type Solid Solution La, 35 (2011) 1899–1907. doi:10.1149/1.3570179.
- [74] R. Krishna, J. A. Wesselingh, The Maxwell-Stefan approach to mass transfer, Chem. Eng. Sci. 52 (1997) 861–911. doi:10.1016/S0009-2509(96)00458-7.
- [75] W. E. Lorensen, H. E. Cline, A High Resolution 3D Surface Construction Algorithm, ACM Trans. Graph. 21 (1987) 163–169.
- [76] D. Kanno, N. Shikazono, N. Takagi, K. Matsuzaki, N. Kasagi, Evaluation of SOFC anode polarization simulation using three-dimensional microstructures reconstructed by FIB tomography, Electrochim. Acta. 56 (2011) 4015–4021. doi:10.1016/j.electacta.2011.02.010.
- [77] Q. Cai, C. S. Adjiman, N.P. Brandon, Investigation of the active thickness of solid oxide fuel cell electrodes using a 3D microstructure model, Electrochim. Acta. 56 (2011) 10809–10811. doi:10.1016/j.electacta.2011.06.105.
- [78] P. A. Connor, X. Yue, C. D. Savaniu, R. Price, G. Triantafyllou, M. Cassidy, G. Kerherve, D. J. Payne, R. C. Maher, L. F. Cohen, R. I. Tomov, B. A. Glowacki, R. V. Kumar, J. T. S. Irvine, Tailoring SOFC Electrode Microstructures for Improved Performance, Adv. Energy Mater. 8 (2018) 1–20. doi:10.1002/aenm.201800120.
- [79] K. Sato, T. Kinoshita, H. Abe, Performance and durability of nanostructured (La_{0.85}Sr_{0.15})_{0.98}MnO₃/yttria-stabilized zirconia cathodes for intermediate-temperature solid oxide fuel cells, J. Power Sources. 195 (2010) 4114–4118. doi:10.1016/j.jpowsour.2010.01.045.
- [80] W.G. Wang, Y.-L. Liu, R. Barfod, S.B. Schougaard, P. Gordes, S. Ramousse, P.V. Hendriksen, M. Mogensen, Nanostructured Lanthanum Manganate Composite Cathode, Electrochem. Solid-State Lett. 8 (2005) A619. doi:10.1149/1.2081890.
- [81] K. Sato, M. Arai, J.C. Valmalette, H. Abe, Surface Capping-Assisted Hydrothermal Growth of Gadolinium-Doped CeO₂ Nanocrystals Dispersible in

- Aqueous Solutions, *Langmuir*. 30 (2014) 12049–12056. doi:10.1021/la502861k.
- [82] Y. Chen, Y. Bu, B. Zhao, Y. Zhang, D. Ding, R. Hu, T. Wei, B. Rainwater, Y. Ding, F. Chen, C. Yang, J. Liu, M. Liu, A durable, high-performance hollow-nanofiber cathode for intermediate-temperature fuel cells, *Nano Energy*. 26 (2016) 90–99. doi:10.1016/j.nanoen.2016.05.001.
- [83] M. Zhang, T. Li, Z. Li, Y. Xing, X. Zhao, M. Shahid, Y. Yuan, H. Nishijima, W. Pan, Enhanced Oxygen Ion Conductivity in Composite Film Electrolytes with Aligned Nanowires, *Adv. Mater. Interfaces*. 5 (2018) 1–5. doi:10.1002/admi.201800098.
- [84] A. He, T. Shimura, J. Gong, N. Shikazono, Numerical simulation of $\text{La}_{0.6}\text{Sr}_{0.4}\text{Co}_{0.2}\text{Fe}_{0.8}\text{O}_3\text{-Gd}_{0.1}\text{Ce}_{0.9}\text{O}_{1.95}$ composite cathodes with micro pillars. *Int. J. Hydrogen Energy*, 44(13) (2019), 6871-6885. doi: <https://doi.org/10.1016/j.ijhydene.2019.01.171>

Acknowledgements

This research is based on my three-year PhD course along with my two-years master course in Shikazono Lab. I am really appreciated for every lab member, and everyone is greatly helpful for my study and life.

Professor Shikazono supervised me all along my 5-year study in the lab. Five years ago, I was not familiar with the numerical simulation and was poor at research presentations. Professor Shikazono was very patient to teach me from the very beginning. When I encountered trouble to solve the PhD program in D2, Professor Shikazono asked me to change my program in time. What is more, Professor Shikazono helped me a lot in my life in Japan. I can never forget the kindness of him.

Ms. Mori and Ms. Hara are the secretaries in Shikazono lab, they have helped me a lot in my daily life. They are always helpful when I had troubles. What is more, I could always receive the Postcard from Ms. Mori during the new year during my staying in Japan. With their help, I never felt lonely in this country. Ms. Yoshida is sitting next to me for about five years, she is very kind and very patient toward her work.

Dr. Onishi helped me a lot in my PhD course. I could never finish the optimization program without his help. When I encountered trouble in programming, he was always able to help me and solve my problem. What is more, he helped me a lot to use the clusters.

Dr. Jiao now became a professor in a university in China. I have studied with him for more than 4 years. And very fortunately, I had one chance to work deeply together with him, but I failed to solve the problem in gas diffusion in the anode side. When communicating with him in the casual time, I learned a lot from him. And I will give my best wishes to him.

Prof. Hara is now teaching at a university in Chiba, I learned a lot with him during the first year when I was a master student. I thought he is the one who can treat the research very seriously, I admire him a lot.

Dr. Kim is the one who treat me as a true friend in Japan. I have helped him during his simulation, he also helped me during my experiment. I thought cooperating with him is exciting and interesting. I hope he is having a good time in Korea.

Dr. Komatsu is really a great researcher and helped my life in Tokyo. His seat is beside me, and he always find my trouble and helps me to solve the trouble. For example, he can always suggest me to access very helpful software. He always works hard in the Lab, which makes me feel guilty when I take a relax.

Dr. Sciazko is also very ready to help others in trouble. Specifically, she patiently taught me to fabricate the cell electrodes. I thought Dr. Komatsu and Dr. Sciazko are good couple, and they will have a good time in the future.

Dr. Yan and Dr. Gong is the Chinese researchers in our lab. They are all talented with academic research, I always talk to them in the spare time. They are kind and helpful. When I encountered troubles in my research or in my life, they can always help me to solve the problems.

Dr. Wang just came to our lab. Maybe I and Dr. Wang will have some cooperation in life and in researches.

Dr. Youn came from South Korea, he told me many stories about South Korea, and I have been with him in Shin-Okubo to eat the Korean Karage. It was very delicious. I stayed in the lab very late at night those days, and I remembered he was always there until 23:00, his hardworking encouraged me a lot.

Mr. Ohi, Mr. Yokoyama, and Mr. Zhou worked with me at my first half year in Todai. Maybe I did not leave a good impression on them because I was not familiar with the life in Tokyo in those days. However, they have helped me a lot. Mr. Ohi helped me to get to know the LBM programming, Mr. Zhou led me to do a lot of administrative work when registration. Mr. Yokoyama helped me to deal with my computer. Now, they have been working in industries for several years. I will give my best wishes to them.

Mr. Ishida and Mr. Fujie are friends of mine. They talked a lot to me in my spare time, from the history to research, from the politics to science. We discussed everything. I learned a lot from them, and maybe we have chance to meet again.

Mr. Saito is a quiet and hardworking guy in the lab. He came from Kyushu, and